Title

Tumor nutrient stress gives rise to a drug tolerant cell state in pancreatic cancer

Authors

Colin Sheehan[1], Lyndon Hu[1*], Guillaume Cognet[1*], Grace Croley[1*], Thao Trang Nguyen[2], Anika Thomas-Toth[2], Darby Agovino[1], Patrick B. Jonker[1], Mumina Sadullozoda[1], Leah M. Ziolkowski[1], James K. Martin 2nd[1,3], Alica K. Beutel[4,5], Ranya Dano[6], Mohammed A. Khan[6], Christopher J. Halbrook[4], Kay F. Macleod[1], Christopher R. Weber[6], James L. LaBelle[2] and Alexander Muir[1#]

[1] Ben May Department for Cancer Research, University of Chicago, Chicago, IL, USA, 60637.
[2] Department of Pediatrics, Section of Hematology/Oncology, University of Chicago, Chicago, IL, USA, 60637.
[3] Department of Cell and Molecular Biology, Rowan-Virtua School of Osteopathic Medicine, Stratford, NJ, USA 08084.
[4] Department of Molecular Biology and Biochemistry, University of California, Irvine, California, USA, 92697.
[5] Department of Internal Medicine I, University Hospital Ulm, Ulm, Germany.
[6] Department of Pathology, University of Chicago, Chicago, IL, USA, 60637.
* These authors contributed equally
[#] Correspondence: amuir@uchicago.edu

Abstract

Cytotoxic chemotherapy remains the standard-of-care treatment for patients with pancreatic ductal adenocarcinoma (PDAC). However, chemotherapy only has modest effects at improving patient survival due to primary or rapidly acquired chemoresistance. The biological underpinnings of PDAC therapy resistance are incompletely defined, but the tumor microenvironment is known to be a major contributor to chemoresistance. We have found chemoresistance is imprinted on PDAC cells by the tumor microenvironment and persists for a period of days after PDAC cells are removed from tumors. However, PDAC chemoresistance is lost upon long term culture in standard laboratory conditions. Interestingly, culture of PDAC cells in Tumor Interstitial Fluid Medium (TIFM), a culture medium we developed to recapitulate the nutrient availability of the tumor microenvironment, maintains PDAC cells in a chemo- and targeted therapy resistant state even after long term culture *ex vivo*. These findings suggest that microenvironmental metabolic stress keeps PDAC cells in a physiologically relevant, therapy resistant cell state that standard culture models fail to maintain. Using TIFM culture, we sought to understand how PDAC cells in this state resist therapeutic challenge. We found that chemo- and targeted therapies largely retain on-target activity within TIFM medium but fail to activate cell death, enabling a “chemotolerant” cell state, which is also observed in PDAC tumors. This chemotolerant state is driven by suppression of apoptotic priming and can be overcome by targeting the anti-apoptotic regulator BCL-XL. Taken together, these findings suggest that reprogramming of cell death mechanisms by the PDAC nutrient microenvironment is a key contributor to therapy resistance in this disease.

Introduction

Pancreatic ductal adenocarcinoma (PDAC) remains one of the deadliest malignancies with a 5-year survival rate of only 12% (*American Cancer Society. Cancer Facts & Figures 2023*, 2023). The low survival rate is driven by the inability to surgically resect most PDACs and chemoresistance exhibited by non-resected tumors (Zeng et al., 2019). Indeed, the majority of PDAC patients exhibit primary resistance to aggressive combination chemotherapy regimens such as gemcitabine and nab-paclitaxel or FOLFIRINOX (fluorouracil, irinotecan and oxaliplatin) (Conroy et al., 2011; Oberstein and Olive, 2013; Von Hoff et al., 2013). Only the minority of patients displayed objective tumor responses according to RECIST criteria (31% for FOLFIRINOX and 23% for gemcitabine and nab-paclitaxel, respectively) with complete responses rarely reported (Conroy et al., 2011; Von Hoff et al., 2013). More recently, KRAS inhibitors, which target the most common oncogenic driver in

PDAC (>90% of cases), have shown efficacy in the treatment of murine (Hallin et al., 2022; Kemp et al., 2023; Wasko et al., 2024) and human (Strickler et al., 2023) PDAC. However, resistance is common (Dilly et al., 2024). Thus, the inability to control PDACs with chemotherapies and targeted therapies remains a significant barrier to the effective management of this disease.

What causes PDAC therapy resistance? Recent studies from human and mouse PDAC point to a critical role of the tumor microenvironment (TME) in driving chemoresistance in PDAC (Beatty et al., 2021). For example, while patients largely do not respond to chemotherapies (Conroy et al., 2011; Von Hoff et al., 2013), cultured human PDAC cells are eradicated by low doses of these drugs (Masoud et al., 2020). Similarly, both genetically engineered and orthotopic allograft mouse models of PDAC are highly resistant to chemotherapeutics (Erstad et al., 2018; Li et al., 2019; Olive et al., 2009), but cell lines established from these models respond to low doses of these drugs (Halbrook et al., 2019). Thus, both human and murine PDAC cells are not inherently chemoresistant. Rather, chemoresistance must be imparted upon PDAC cells by one or more factors present within the TME.

The PDAC TME is known to inhibit chemotherapy response by impairing the ability of drugs to access PDAC cells. A well-established feature of PDAC tumors is dramatic desmoplasia, resulting in a stromal compartment that significantly outnumbers malignant cells in the tumor (Feig et al., 2012). Pressure from the stroma can compress blood vessels, which limits perfusion and drug delivery to PDAC tumors (Chauhan et al., 2014; Jacobetz et al., 2013; Olive et al., 2009; Provenzano et al., 2012; Stylianopoulos et al., 2012). Additionally, stromal cells can accumulate drugs (Hessmann et al., 2018) and secrete metabolites that block drug uptake by cancer cells (Dalin et al., 2019; Halbrook et al., 2019). Thus, multiple mechanisms are operative in the TME that limit drug exposure in PDAC cells, which led to the hypothesis that PDAC desmoplasia and impaired drug delivery are key mediators of chemoresistance in this disease (Hosein et al., 2020). However, recent preclinical and clinical studies have shown that direct delivery of therapeutic agents to the tumor parenchyma (Levy et al., 2017) and agents targeting the PDAC desmoplastic reaction (Amakye et al., 2013; Özdemir et al., 2014; Ramanathan et al., 2019; Rhim et al., 2014; Tempero et al., 2020) do not improve outcomes. Additionally, recent work in preclinical pancreatic cancer models indicates that chemotherapies do penetrate into PDAC tumors and engage their targets, but nevertheless fail to alter tumor progression (Kramer et al., 2015; Strittmatter et al., 2022). For example, murine tumors treated with genotoxic PDAC chemotherapies do exhibit DNA damage markers such as γH2AX, but tumors do not show evidence of cancer cell death and grow as well as untreated tumors (Halbrook et al., 2019; Knight et al., 2017; Strittmatter et al., 2022). Together, these results argue for the existence of additional mechanisms by which the TME causes chemoresistance, beyond being a barrier to drug delivery (Hakim et al., 2019).

In this study, we sought to understand the additional mechanisms by which the TME impairs chemotherapy response in PDAC. We found that PDAC cells freshly isolated from chemotherapy resistant tumors were drug resistant upon initial isolation, but that therapy resistance was lost in PDAC cells upon extended culture in standard laboratory conditions. In contrast, PDAC cells cultured in Tumor Interstitial Fluid Medium (TIFM), a culture medium that recapitulates the nutrient availability of the TME, were resistant to both targeted and chemotherapies even after long term culture. Therapy resistance in PDAC cells freshly isolated from tumors or cultured in TIFM was not driven by suppression of drug activity, but rather by tolerance of PDAC cells to cytotoxic stress induced by therapeutics. This “chemotolerant” phenotype was enabled by suppression of apoptotic priming in PDAC cells and could be overcome by targeting the anti-apoptotic regulator BCL-XL. Taken together, these studies indicate that the nutrient TME is a major contributor to therapy failure in PDAC by imprinting a state of suppressed apoptotic priming that enables PDAC cells to tolerate drug-induced cytotoxic stress.

Results

The tumor microenvironment imprints chemotherapy resistance in PDAC cells

To understand how the TME contributes to chemotherapy resistance in PDAC, we used a previously described (Halbrook et al., 2019) model of TME-induced drug resistance. In this model, PDAC cells derived from autochthonous murine PDAC tumors, which are chemosensitive in culture, are used to generate chemotherapy resistant orthotopic allograft tumors in mice (Fig. 1A). We previously established murine PDAC cell lines in standard cell culture medium (RPMI-1640; termed mPDAC-RPMI lines) from the C57Bl6J *Kras*$^{LSL\text{-}G12D/+}$; *Trp53*$^{fl/fl}$; *Pdx1*^{Cre} (*KP*$^{-/-}$*C*) mouse model of PDAC (Apiz Saab et al., 2023). We found that mPDAC3-RPMI cells are highly sensitive to low doses of the PDAC chemotherapeutic agent gemcitabine in culture (Fig. 1B). In contrast, when we implanted mPDAC3-RPMI cells to form orthotopic PDAC tumors in mice, gemcitabine displays limited efficacy at reducing tumor burden (Fig. 1C), even when given at a dose beyond what has previously been found to lead to intratumoral drug accumulation and DNA damage in murine PDAC tumors (Strittmatter et al., 2022). Thus, PDAC cells are not innately chemotherapy resistant but require interaction with the TME to become drug resistant.

We then asked whether the PDAC cells removed from the TME would maintain drug resistance or become sensitive. To do so, we split a culture of mPDAC3-RPMI cells and either continuously cultured the cells in RPMI or generated tumors in mice (tumor-adapted cells). We then isolated PDAC cells from the tumors by fluorescence-activated cell sorting (FACS) using the established PDAC cell marker mesothelin (Argani et al., 2001; Guo et al., 2025; O'Hara et al., 2016) and assessed the response of these cells to treatment with gemcitabine or SN-38 (the active metabolite of irinotecan, a chemotherapeutic agent used in PDAC treatment) after different lengths of time in standard culture (Fig. 1D). Interestingly, we found that tumor-adapted cells were significantly more resistant to chemotherapies compared to parental mPDAC3-RPMI cells (Fig. 1E,F). However, after prolonged culture in RPMI, tumor-adapted cells no longer exhibited enhanced drug resistance (Fig. 1E,F). Collectively, these results demonstrate that the TME temporarily imprints a chemotherapy resistant state in PDAC cells, but which is lost upon prolonged culture in standard laboratory conditions.

Tumor nutrient conditions are sufficient to imprint therapy resistance in PDAC

We next asked which components of the TME imprint the chemotherapy resistant state in PDAC cells. Given recent studies that have highlighted the contribution of the nutrient or metabolic microenvironment to drug response (Abbott et al., 2023; Flickinger et al., 2024; Gonçalves et al., 2021; Muir and Vander Heiden, 2018; Rawat et al., 2024; Sela et al., 2022; Sheehan and Muir, 2025) and cellular state (García-Jiménez and Goding, 2019; Mancini et al., 2023; Wang et al., 2024), we hypothesized that TME nutrient availability may be a critical contributor to TME-imprinted drug resistance. To determine if tumor nutrient conditions can imprint drug resistance in PDAC cells, we measured the response of paired mPDAC cell lines that are cultured in either standard media (RPMI) or in Tumor Interstitial Fluid Medium (TIFM; mPDAC-TIFM cells), a cell culture medium containing nutrients at the levels measured in the PDAC TME (Apiz Saab et al., 2023) (Fig. 2A). We found that PDAC cells in TIFM were more resistant to a panel of standard-of-care chemotherapies with diverse mechanisms of action compared to PDAC cells cultured in RPMI (Fig. 2B-E and Fig. 2 Figure Supplement 1A-B). Interestingly, PDAC cells in TIFM also exhibited decreased sensitivity to targeted therapies that inhibit RAS signaling (Fig. 2F and Fig. 2 Figure Supplement 1C). Lastly, we asked if deriving organoids in TIFM would likewise affect therapy response for patient-derived PDAC specimens. We generated paired patient-derived organoid cultures in standard media or TIFM and found organoids cultured in TIFM were significantly more resistant to gemcitabine challenge than organoids grown in standard organoid media (Fig. 2 Figure Supplement 1D). Altogether, these data indicate that both murine and human PDAC cultures derived in TIFM exist in a chemotherapeutic resistant state.

One potential explanation for TIFM-conferred drug resistance is that mPDAC cells proliferate slower in TIFM and many chemotherapeutics target actively cycling cancer cells (Letai and de The, 2024; Shah and Schwartz, 2001). Although mPDAC-TIFM cells proliferate slower than mPDAC-RPMI cells (Apiz Saab et al., 2023; Jonker et al., 2025) and have a reduced proportion of cells in S-phase by EdU incorporation (Fig. 2 Figure Supplement 2A), mPDAC-TIFM cultures remain significantly less sensitive to chemotherapeutic agents even after correcting for differences in cycling rate using previously described methods (Hafner et al., 2016) (Fig. 2 Figure

Supplement 2B-F). Additionally, when mPDAC-TIFM cells were exposed to gemcitabine, which causes actively cycling cells to arrest in S-phase (Montano et al., 2017), the vast majority of the cell population could be observed to be trapped in S-phase within 24 hours of drug exposure (Fig. 2 Figure Supplement 2G). However, mPDAC-TIFM cells remain viable beyond 72 hours of continuous drug treatment (Fig. 2B-F). Lastly, slowing the growth rate of mPDAC-RPMI cultures to that of mPDAC-TIFM cultures through CDK4/6 inhibition does not induce the level of drug resistance observed in mPDAC-TIFM cultures (Fig. 2 Figure Supplement 2H,I). In total these findings indicate that therapeutic resistance in mPDAC-TIFM cultures cannot be accounted for by slower proliferative kinetics.

A second potential explanation for the TIFM-induced drug resistance phenotype is that PDAC cells undergo different cell fates following drug exposure dependent on their nutrient environment, wherein mPDAC-RPMI cells undergo cell death while mPDAC-TIFM cells lose proliferative potential and undergo senescence (Childs et al., 2014). We observed that mPDAC-TIFM cultures not only display increased viability throughout chemotherapy exposure (Fig. 2B-F), but that these cultures resume proliferation following drug removal, in contrast to RPMI cultured cells (Fig. 2 Figure Supplement 3A). Thus, TIFM-cultured PDAC cells maintain viability and proliferative potential upon chemotherapeutic challenge.

We next asked if the chemoresistance phenotype exhibited by mPDAC-TIFM cells would be lost upon culturing these cells in RPMI, as we had previously observed with tumor-adapted PDAC cells (Fig. 1E,F). Indeed, while mPDAC-TIFM cells cultured in RPMI are initially resistant to chemotherapeutic challenge, prolonged culture in RPMI gradually sensitizes cells to chemotherapeutics (Fig. 2G,H). Thus, TME-imprinted therapy resistance is maintained by culturing PDAC cells in TIFM, but is lost over time when cells are transferred into standard culture conditions.

The finding that culture in TIFM could maintain PDAC cells isolated from tumors in a chemoresistant state prompted us to ask if TIFM culture could induce therapy resistance in chemosensitive PDAC cell lines initially derived in standard culture conditions. We previously found that mPDAC-RPMI cultures could not immediately proliferate when transferred into TIFM (Apiz Saab et al., 2023), However, mPDAC-RPMI cells could be transitioned to grow in TIFM over time by growing cultures in mixtures of TIFM and RPMI, increasing the ratio of TIFM:RPMI as cultures adapted and proliferated (Fig. 2I). We similarly transitioned human PDAC cell lines and organoids derived in standard culture conditions to grow in TIFM (Fig. 2I). We then assessed the response of TIFM-transitioned PDAC cells to chemotherapeutic challenge. TIFM-transitioned mPDAC cultures (Fig. 2J), human PDAC organoids (Fig. 2K) and human PDAC cell lines (Fig. 2L-N) were more resistant to chemotherapeutic exposure than parental cells maintained in RPMI. Thus, TIFM exposure, like exposure to the complete PDAC TME, is sufficient to induce chemotherapeutic resistance in PDAC cells.

Given the limited ability of mPDAC-RPMI cells to initially grow in TIFM, we asked if adaptation to TIFM results in clonal selection for rare PDAC subpopulations that are both chemoresistant and able to grow in TIFM. Using lentiviral barcoding (Bhang et al., 2015), we transitioned a population of mPDAC-RPMI cells into TIFM or maintained these cells in RPMI, and assessed clonal diversity after 17 population doublings (Fig. 2 Figure Supplement 4A). We found that culture of mPDAC cells in standard conditions led to a loss of clonal diversity similar to what has been previously observed in other cancer cell lines (Bhang et al., 2015). Transitioning mPDAC-RPMI cells into TIFM only modestly increased this loss of clonal diversity (Fig. 2 Figure Supplement 4B-C). Additionally, we assessed the change in abundance of individual mPDAC clones by measuring the change in abundance of individual barcodes after culture in RPMI or transition to TIFM. We found that changes in barcode abundance were strongly correlated between the two culture conditions (Fig. 2 Figure Supplement 4D), suggesting that both RPMI conditions and transitioning to TIFM select for the same mPDAC clones. Thus, TIFM does not select for a rare subset of drug resistant clones but rather induces this phenotype in the majority of mPDAC cells.

TME nutrient stress induces chemotolerance by suppressing apoptotic priming

Similar to TME exposure, culture in TIFM induces therapy resistance in PDAC cells. Therefore, we used the tractable *in vitro* TIFM model to probe the mechanisms underlying PDAC chemoresistance. To understand how TIFM cultured cells survive chemotherapeutic challenge, we first determined the cell death mechanism by which chemotherapies kill PDAC cells. Chemotherapies are known to kill cancer cells in an apoptosis-dependent manner, but at times other mechanisms can be engaged (Hänggi and Ruffell, 2023; Strasser and Vaux, 2020). CRISPR-mediated knockout of *Bax* and *Bak1*, key effectors of mitochondrial-dependent apoptosis, prevented mPDAC-RPMI cell death upon chemotherapeutic challenge (Fig. 3A). Therefore, we conclude that chemotherapeutic challenge kills mPDAC cells via mitochondrial-dependent apoptosis.

We next asked which step of the apoptotic cascade was impaired in TIFM-cultured PDAC cells (Fig. 3B). We first assessed if chemotherapeutic damage of PDAC cells was impaired by TIFM culture. Gemcitabine, 5-Fluorouracil (5-FU) and SN-38 are all drugs that generate DNA damage as part of their anti-cancer effects (Vincent T. DeVita, Jr., Theodore S. Lawrence, Steven A. Rosenberg, 2015). Therefore, we assessed DNA damage in PDAC cells after drug exposure by alkaline comet assay and induction of γH2AX. Gemcitabine and SN-38 generated similar degrees of DNA damage in TIFM and RPMI cultures, indicating that TIFM culture does not impair chemotherapeutic action (Fig. 3C,F and Fig. 3 Figure Supplement 1A-C). In contrast, induction of DNA breaks and γH2AX by 5-FU was impaired in TIFM (Fig. 3 Figure Supplement 2A,B). The cytotoxicity of 5-FU is in part mediated by inhibition of thymidylate synthase (Martin et al., 1980; Mullen and Singh, 2023; Wilson et al., 2014) and exogenous availability of thymidine is known to alleviate the cytotoxicity of 5-FU (Flickinger et al., 2024; Piper et al., 1983; Yan et al., 2016) by restoring thymidine concentrations and enabling DNA replication (Fig. 3 Figure Supplement 2C). TIFM contains 2.25 μM thymidine (Apiz Saab et al., 2023), so we asked if exogenous thymidine was responsible for the observed resistance to 5-FU we observed in TIFM. We found that supplementing mPDAC-RPMI cultures with TIFM levels of thymidine rescued DNA damage induced by 5-FU (Fig. 3 Figure Supplement 2B) and cell viability (Fig. 3 Figure Supplement 2D). Lastly, we observed that TIFM culture did not impact the ability of KRAS-targeted therapies to inhibit RAS signaling (Fig. 3 Figure Supplement 3A). Together, these results indicate that TIFM culture, with the exception of 5-FU, does not significantly disrupt the biochemical action of chemo- and targeted therapies in PDAC cells. Therefore, we conclude that TIFM-culture causes chemoresistance by enabling cells to persist despite the induction of chemotherapeutic stress, a state which we term “chemotolerance”.

Given that TIFM culture protects PDAC cells from therapy induced death by enabling a chemotolerant cell state, we asked whether culturing in TIFM gives rise to changes in stress-induced apoptotic signaling, as dampening stress-induced signaling has been found to limit the cytotoxicity of various cellular stresses (Loukas et al., 2022). Initially, we assessed whether gemcitabine treatment would result in differing transcriptomic responses of PDAC cells based on the medium culture conditions. Comparing gene set enrichment analysis (GSEA) results between the cultures with gemcitabine exposure, we observe induction of similar gene expression programs irrespective of the culture conditions (Figure 3D). Additionally, inference of transcription factor activity based on these gene expression changes indicated that both TIFM and RPMI cells produce a strong JUN and FOS transcriptional signatures, two transcription factors with critical roles in cell death signaling (Davis, 2000; Johnson and Nakamura, 2007; Preston et al., 1996) (Figure 3E). We observed similar trends in transcriptional changes for pro-apoptotic BCL2 family genes in mPDAC cells cultured in TIFM and RPMI, with the strongest upregulation in response to gemcitabine being associated with *Bcl2l11*, encoding the apoptotic activator, BIM (Fig. 3 Figure Supplement 4A). We observed a similar induction of the pro-apoptotic protein BIM by immunoblotting in both TIFM and RPMI cells upon chemotherapy exposure (Figure 3F and Fig. 3 Figure Supplement 1C). Collectively, these results indicate that culture in TIFM does not substantially impair sensing of chemotherapeutic stress by PDAC cells or the induction of pro-apoptotic signals in response to therapy challenge.

The next step in therapy-induced apoptosis is mitochondrial outer membrane permeabilization (MOMP) and cellular destruction triggered by the activation of executioner caspases (Fig. 3B). We assessed MOMP induction using two approaches. First, using a genetically-encoded sensor of mitochondrial integrity (Tait et al., 2010), we found that MOMP readily occurred in mPDAC-RPMI cultures challenged with gemcitabine, but not

mPDAC-TIFM cells (Fig. 3G,H). Second, MOMP activation is triggered by the oligomerization of pore-forming proteins such as BAK and BAX at the mitochondria, which are continuously retrotranslocated back to the cytosol under homeostatic conditions (Edlich et al., 2011; Todt et al., 2015). Using subcellular fractionation, we observed that BAX translocated from the cytosol to the mitochondria with gemcitabine treatment in RPMI, but not TIFM cells (Figure 3I). Lastly, we assessed caspase activation in mPDAC cultures upon gemcitabine treatment. mPDAC-RPMI, but not mPDAC-TIFM cultures, exhibited robust caspase activation upon chemotherapeutic treatment (Fig. 3F and Fig. 3 Figure Supplement 1C). These data indicate that TIFM culture limits MOMP in response to chemotherapeutic stress. MOMP activation is determined by the balance of pro- and anti-apoptotic BCL2 family genes. How close this balance is towards tipping in favor of MOMP is referred to as cellular apoptotic priming (Kale et al., 2018; Potter and Letai, 2016). Apoptotic priming can be directly assayed in cells by monitoring changes in mitochondrial polarization in response to the application of BH3-only peptides. We observed that mPDAC-TIFM cells indeed exhibited limited mitochondrial depolarization in response to recombinant BIM peptide compared to mPDAC-RPMI cells, consistent with decreased apoptotic priming under TIFM culture conditions (Fig. 3J). We then asked whether highly primed mPDAC-RPMI cultures transitioned to grow in TIFM would similarly gain chemotolerance and reduced apoptotic priming. Indeed, RPMI cells transitioned into TIFM exhibited limited caspase-3 activation in response to gemcitabine despite induction of DNA damage and BH3 only proteins (Fig. 3 Figure Supplement 5A,B). Additionally, RPMI cells transitioned into TIFM required significantly higher concentrations of recombinant BIM peptide to trigger mitochondrial depolarization relative to the RPMI parental culture (Fig. 3 Figure Supplement 5C). Given the transferability of chemotolerance and apoptotic priming with the TIFM medium, one outstanding question is what specific nutrient(s) present in the medium enable chemotolerance and altered apoptotic priming in PDAC cells. Previous analysis of PDAC TIF identified amino acid depletion, in particular depletion of the amino acid arginine, as a significant TME metabolic stress to which PDAC cells must adapt (Apiz Saab et al., 2023; Jonker et al., 2025; Lee et al., 2023; Menjivar et al., 2023). Therefore, we asked if arginine starvation could similarly give rise to the chemotolerant cell state PDAC cells by transitioning mPDAC-RPMI cells to grow in RPMI medium with TME levels of arginine (10 μM) (Fig. 3 Figure Supplement 5D). mPDAC cells cultured in low arginine conditions also demonstrated limited caspase-3 activation despite induction of DNA damage with gemcitabine (Fig. 3 Figure Supplement 5E). Furthermore, mPDAC cells cultured in low arginine conditions exhibited reduced apoptotic priming (Fig. 3 Figure Supplement 5F). Thus, these data suggest that chronic nutrient stress promotes chemotolerance via reduced apoptotic priming in PDAC.

Lastly, we wanted to assess if reduced apoptotic priming in TIFM was critical for therapy resistance in PDAC cells cultured under these conditions. To ask this, we first sought to determine which anti-apoptotic proteins PDAC cells utilize to suppress apoptosis. mPDAC cells uniformly expressed BCL-XL and MCL-1, but not BCL-2 (Fig. 3K). Therefore, we sought to determine if BCL-XL or MCL-1 were responsible for suppressing apoptosis in mPDAC cells. We immunoprecipitated BCL-XL and MCL-1 from mPDAC1-RPMI cells and found that only BCL-XL co-immunoprecipitated with the pro-apoptotic proteins BIM and BAX (Fig. 3L). These results suggested that BCL-XL is the primary anti-apoptotic protein in mPDAC cells, as has previously been reported for both pancreatic progenitor and PDAC cells (Ikezawa et al., 2017; Loo et al., 2020; Sela et al., 2022; Thummuri et al., 2022; Zhang et al., 2025). We next found the BCL-XL interaction with BAX was not impacted in gemcitabine-treated mPDAC-TIFM cultures but was reduced in treated mPDAC-RPMI cultures (Fig. 3M), consistent with reduced apoptotic priming in mPDAC-TIFM cultures driven by enhanced BCL-XL function. The interaction between BCL-XL and BAX was fully lost in both cultures upon treatment with the BCL-XL-targeting BH3 mimetic A1331852 (Fig. 3M). We next asked if targeting BCL-XL in TIFM cultured mPDAC cells could overcome therapy resistance in these cultures. We treated cells with the following BH3-mimetic compounds targeting specific anti-apoptotic proteins and assessed the ability of these compounds to enhance the cytotoxicity of gemcitabine in TIFM cultures: venetoclax (BCL-2 specific), navitoclax (BCL-XL and BCL-2 specific), A1331852 (BCL-XL specific), and S63845 (MCL-1 specific). We consistently observed a synergistic interaction between gemcitabine and the BCL-XL targeting mimetics, but not mimetics that target other anti-apoptotic proteins (Fig. 3N). Additionally, *Mcl1* overexpression abrogated the synergy of BCL-XL targeting mimetics and gemcitabine in mPDAC-TIFM cultures (Fig. 3 Figure Supplement 6A), suggesting the synergy observed between BH3 mimetics and gemcitabine in TIFM is primarily driven by the effect of BCL-XL on

apoptosis and not non-apoptotic functions of BCL-XL that MCL-1 cannot replace (Choi et al., 2016; Sela et al., 2022; Zhang et al., 2024). To confirm the role of BCL-XL in cell survival under chemotherapeutic stress in TIFM, we utilized CRISPR to knockout *Bcl-xL* from mPDAC-TIFM cells (Fig. 3O). When exposed to gemcitabine, *Bcl-xL*-KO cells had a markedly reduced survival, similar to that of mPDAC-RPMI cultures (Fig. 3O). In addition, via immunoblotting for cleaved-caspase-3, we observed *Bcl-xL*-KO cells had active caspase-3 upon gemcitabine treatment, which we did not observe in control mPDAC-TIFM cultures (Fig. 3P). Altogether, these data suggest that TIFM cultures are chemotolerant due to reduced apoptotic priming that is dependent on BCL-XL activity.

The tumor microenvironment imprints a chemotolerant phenotype on PDAC cells

The previous results indicate that TIFM culture pushes PDAC cells into a chemotolerant state that enables cells to survive chemotherapeutic stress due to lower apoptotic priming. We asked if similar processes occurred *in vivo* and contributes to TME-induced drug resistance. We treated therapy-resistant murine orthotopic tumors with gemcitabine as previously described (Fig. 1C) and assessed tumors for markers of DNA damage (γH2AX) and apoptosis (cleaved caspase-3) (Figure 4A). While gemcitabine treated tumors showed a robust induction of DNA damage, indicating on-target gemcitabine activity, we were unable to detect any change in the presence of cleaved caspase-3 (Fig. 4B-D). Thus, these results suggest PDAC tumors display chemotolerance, wherein chemotherapy drugs maintain on-target activity, but have minimal cytotoxic effects.

Finally, we asked if a change in apoptotic priming occurred in TME-imprinted chemotolerance, as we had observed in TIFM-cultured PDAC cells. To assess this, we collected cancer cells by FACS from murine orthotopic tumors as previously described (Fig. 1D) and measured their apoptotic priming by BH3 profiling compared to parental mPDAC-RPMI cultures (Fig. 4E). PDAC cells isolated from tumors were significantly less primed relative to cells that were maintained in standard culture conditions (Fig. 4F). In addition, as with chemotherapy resistance (Fig. 1E,F), prolonged culture in standard media reverted the decrease in apoptotic priming that TME exposure induced (Fig. 4G). Thus, like TIFM, the TME imprints a chemotolerant state with lowered apoptotic potential on PDAC cells.

Discussion

Chemotolerance is an important contributor to therapy resistance in PDAC

The TME is known to be a driver of therapy resistance in PDAC (Beatty et al., 2021; Sherman and Beatty, 2022), but the mechanistic basis behind TME-induction of therapy resistance has not been fully elucidated. One proposed critical mechanism by which the TME causes drug resistance is that stromal desmoplasia prevents the delivery of therapeutic agents to the tumor (Hosein et al., 2020). However, preclinical studies measuring gemcitabine delivery within PDAC tumor (Kramer et al., 2015; Strittmatter et al., 2022) and clinical studies measuring the impact of targeting stromal desmoplasia on patient outcomes when treated with chemotherapeutics (Amakye et al., 2013; Özdemir et al., 2014; Ramanathan et al., 2019; Rhim et al., 2014; Tempero et al., 2020) suggest that the TME must contribute to therapy resistance via other mechanisms. In similar findings to others (Halbrook et al., 2019), we found that when we implanted chemotherapy-sensitive cancer cells to form PDAC tumors in mice, the resulting tumors were largely unresponsive to the same chemotherapeutic treatment, consistent with the TME playing a fundamental role in therapy resistance in this disease. We then further isolated these tumor-adapted PDAC cells from tumors and found they displayed substantially reduced sensitivity to chemotherapy agents in culture compared to the parental culture from which they were derived. These findings demonstrate at least some of the resistance brought by the TME must be due to characteristics imprinted on PDAC cells that persist for a period of time even after the TME has been removed.

We sought to understand how the TME reprogrammed PDAC cells to resist therapeutic treatment. PDAC cells isolated from tumors do not evade the biochemical action of therapeutics but instead dampen apoptotic priming

to the extent that the PDAC cells no longer die when experiencing therapy-induced stress. Thus, tumor adapted cells are tolerant of therapeutic stress, a state we term chemotolerant. We additionally observed evidence of chemotolerance in animal tumors, where chemotherapy treated tumors exhibited evidence of on-target activity but not commitment to cell death. Furthermore, analysis of chemo- and radiotherapy treated patient tumors indicates the presence of therapy tolerant persister cells (Bernard et al., 2025; Zhou et al., 2023). Thus, in addition to limiting therapy delivery in PDAC, the imprinting of a chemotolerant state on cells is an important TME barrier to therapy efficacy in PDAC. Importantly, aside from our findings that PDAC cells rely upon BCL-XL to maintain chemotolerance, we do not understand the molecular basis for reduced apoptotic priming of PDAC cells from tumors. Upregulation of BCL-XL was not consistently observed in our studies of chemotolerant cells, arguing that expression levels of this anti-apoptotic alone are not fundamental to the acquisition of this cell state. Instead, we hypothesize there may be another mode of regulation that promotes the limited apoptotic potential and chemotolerance of these cells, as has been observed in other chemotolerant cell types such as senescent cells (Alcon et al., 2025). Future studies will be needed to understand TME regulation PDAC apoptotic priming and chemotolerance. Nevertheless, our findings that BCL-XL-mediated apoptotic resistance is key to chemotolerance in PDAC is consistent with recent findings that targeting BCL-XL can improve therapeutic outcomes in animal models PDAC (Han et al., 2025; Sela et al., 2022; Thummuri et al., 2022; Zhang et al., 2025) and suggest that targeting critical regulators of chemotolerance could improve efficacy of PDAC treatments.

While our studies have largely focused on PDAC response to cytotoxic chemotherapies, the mechanism of chemotolerance by dampening apoptotic priming is likely to mitigate the response to any therapy that relies on engaging this mode of cell death. Notably, new RAS targeted therapies exert their efficacy at least in part by inducing PDAC cell apoptosis (Becker et al., 2024; Kemp et al., 2023; Li et al., 2025; Mahadevan et al., 2023; Orlen et al., 2025; Wasko et al., 2024). We found that chemotolerant TIFM PDAC cultures also exhibited tolerance to RAS targeted therapies. Furthermore, drug tolerant persister cells lead to relapse of murine PDAC tumors treated with RAS targeted therapies (Broderick et al., 2025). Thus, future studies determining if TME imprinting of low apoptotic potential on PDAC cells contributes to targeted therapy resistance are warranted.

The chemotolerant PDAC cell state is imprinted by the TME but not maintained in standard culture conditions

An interesting feature of PDAC TME-imprinted chemotolerance is the transient nature of this phenotype. PDAC cells isolated from tumors exhibited chemotolerance only for a period of days after isolation from the tumor. This suggests a temporary cellular “memory” of the TME. Such transient cellular memory is frequently encoded epigenetically (D’Urso and Brickner, 2014). Future studies elucidating how the TME epigenetically reprograms PDAC cells will be necessary to understand how the chemotolerant state is imprinted by the TME. Understanding this imprinting could lead to new approaches to limit the development of chemotolerance to improve the efficacy of therapies in PDAC treatment.

The finding that standard culture models cannot maintain PDAC cells in a physiologically relevant chemotolerant state also has important implications for the use of these models in preclinical drug efficacy studies. Culture models have proven useful for identifying genetic determinants of therapy response (Basu et al., 2013; Corsello et al., 2020; Iorio et al., 2016; Shoemaker, 2006), which has been key in the development of precision medicine. However, tumor response to cytotoxic and targeted therapies are often dampened compared to what is predicted from culture models (Scannell et al., 2022). Many explanations for these discrepancies have been put forward including differences in growth rate, phenotypic heterogeneity and differences in drug exposure between cancer cells in culture and in tumors (Scannell et al., 2022). Our data suggests an important additional rationale for differences between drug efficacy observed in culture and in tumors, namely the increased apoptotic priming of PDAC cells in standard culture conditions. Apoptotic priming is a critical determinant of therapy response (Sarosiek et al., 2013). The observation that standard culture conditions increase apoptotic priming of cancer cells could explain why therapies that induce apoptosis often

have stronger effects in culture models than in tumors. This standard culture media-induced shift in apoptotic priming could also limit the predictive power of culture models when used both for drug discovery and as ex vivo precision medicine platforms (Acanda de la Rocha et al., 2025; Beutel et al., 2021; Boilève et al., 2024; Letai, 2017; Letai et al., 2022; Tiriac et al., 2018; van Renterghem et al., 2023; Wensink et al., 2021). Thus, development of culture systems that better represent the tumor microenvironment, and the changes in cell state that the TME confers, will be critical to improve the predictive power of *ex vivo* cancer models.

TME nutrient stress induces a chemotolerant PDAC cell state

Which component of the TME is responsible for reprogramming PDAC cells to the chemotolerant state? PDAC is poorly perfused due to hypovascularity (Hasselluhn et al., 2023; Kahn et al., 2021) and limited functionality of available vessels (Olive et al., 2009; Provenzano et al., 2012). These features of PDAC tumors result in abnormal nutrient levels in the TME (Sheehan and Muir, 2025). Nutrient limitation and metabolic stress is known to select cells with diminished apoptotic potential (Blanco et al., 2016; Graeber et al., 1996; Kim et al., 1997; Ravindran Menon et al., 2015) and been linked to the generation of drug tolerant cancer cells (Mancini et al., 2023). This led us to hypothesize that nutrient stress in the TME could push cells into a state of decreased apoptotic potential resulting in cross-tolerance to apoptosis-inducing therapies. Our finding that TIFM culture induces a chemotolerant state suggests that TME metabolic stress is an important contributor to limited therapy response in PDAC. These findings do not exclude the contribution of other factors in the TME that promote drug resistance but suggest that nutrient stress induced-chemotolerance is a critical barrier to the efficacy of targeted and chemotherapies used for the treatment of PDAC. The induction of chemotolerance by metabolic stress in PDAC tumors may explain why poor perfusion correlates with worse outcomes for PDAC patients (Komar et al., 2009). Future studies identifying the specific metabolic stresses that trigger chemotolerance in PDAC and developing approaches to relieve these stresses PDAC tumors will be necessary to determine the extent to which preventing chronic metabolic stress in the TME can limit the onset of chemotolerance and therapy resistance.

Material and methods

Cell lines and culture

Murine cancer cell lines were derived from *Kras*$^{LSL\text{-}G12D/+}$; *Trp53*$^{fl/fl}$;*Rosa26* $^{tm1(EYFP)Cos}$; *Pdx1*^{Cre} (mPDAC1-3) and the *Kras*$^{FSF\text{-}G12D/+}$;*Trp53*$^{frt/frt}$;*Pdx1*^{Flp} (mPDAC4) autochthonous mouse models of PDAC, and were isolated and cultured as previously described (Apiz Saab et al., 2023). Human cancer cell lines, ASPC1 and 8988T, were generously donated from the lab of Dr. Matthew Vander Heiden. Use of cancer cell lines was approved by the Institutional Biosafety Committee (IBC 1560). All cancer cell lines were tested quarterly for mycoplasma contamination using the Mycoalert Mycoplasma Detection Kit (Lonza, LT07-318). All cells were cultured in Heracell Vios 160i incubators (Thermo Fisher) at 37°C and 5% CO_2. Cell lines were routinely maintained in RPMI-1640 or TIFM supplemented with 10% dialyzed FBS (Gibco, 26400-044).

Generation of mPDAC-RPMI→TIFM and mPDAC-RPMI→low arginine cultures

To generate low arginine medium, RPMI-1640 without amino acids and glucose (US Biological Life Sciences, D9800-27) was supplemented with all amino acids and glucose to RPMI-1640 concentrations, except for arginine which was supplemented at a concentration of 10 μM. Murine cancer cell lines described above were then cultured in this low arginine RPMI media for 6 weeks prior to the start of experiments.

To generate mPDAC-RPMI→TIFM cultures, murine and human PDAC cell lines were initially transferred to a medium environment containing 99% TIFM and 1% RPMI for about 2 weeks until cultures grew to confluency. These cultures were then passaged in 100% TIFM. Cells were then maintained in TIFM for 4 weeks prior to that start of experiments.

Human samples regulation

Human PDAC samples were obtained under approval by the Institutional Review Boards at the University of Chicago (20-1683).

Derivation of patient-derived organoids in TIFM medium

Human pancreatic ductal adenocarcinoma (PDAC) biopsy specimens were obtained under institutional review board–approved protocols with informed patient consent. Fresh tissue was transferred into digestion medium consisting of Advanced DMEM/F12 (Gibco, 12634010) supplemented with 1× penicillin/streptomycin (Gibco, 15140163), 1× GlutaMAX (Gibco, 35050061), 10 mM HEPES (Gibco, 15630080), and 100 µg/mL Primocin (InvivoGen, ant-pm-05), containing 0.125 mg/mL collagenase IV (Sigma-Aldrich, C9407) and 0.125 mg/mL Dispase II (Sigma-Aldrich, D4693). Tissue was minced until the pieces were barely visible by eye, then transferred to 15 mL conical tubes containing digestion medium and incubated for exactly 30 minutes at 37 °C on an orbital shaker set to 100 rpm. Following digestion, the suspension was passed through a pre-wetted 100 µm cell strainer (Falcon, 352360) using a pipette to facilitate passage, and the filtrate was collected into a new tube. The suspension was centrifuged at 500 × g for 5 min at 4 °C, and the pellet was washed in Advanced DMEM/F12 with 1% FBS (Corning, 35-015-CV).

Cells were embedded in pure Cultrex UltiMatrix Reduced Growth Factor Basement Membrane Extract (Bio-Techne, BME001) and plated in two 35 µL domes per well in pre-warmed 24-well plates (Greiner, 662102). Plates were inverted and incubated at 37 °C for 20–30 min before overlaying with 500 µL of complete PDAC organoid medium. The medium comprised TIFM medium supplemented with 10.5 µM Y-27632 (Cayman Chemical, 10005583), 300–360 ng/mL recombinant human Noggin (ImmunoPrecise Antibodies, N002), 800–880 ng/mL recombinant human R-spondin (ImmunoPrecise Antibodies, R001), 1× B27 supplement (Gibco, 17504044), 5 mM nicotinamide (Thermo Scientific, 128271000), 100 µg/mL Primocin (InvivoGen, ant-pm-05), 50 ng/mL recombinant human EGF (PeproTech, AF-100-15), 10 ng/mL heat-stable recombinant human FGF-10 (Gibco, PHG0371), 500 nM A83-01 (BioGems, 9094360), and 100 nM gastrin (Sigma-Aldrich, G9145). Cultures were maintained at 37 °C in a humidified incubator with 5% CO_2, with medium replaced every 2–3 days. Organoids were passaged when the average diameter reached 200–300 µm, using TrypLE with Y-27632, and re-embedded in fresh UltiMatrix domes as above.

Patient-derived organoid derivation in standard organoid conditions

Human PDAC biopsy specimens were obtained from surgical resections under institutional review board–approved protocols with informed patient consent. Organoids were isolated as previously described (Boj et al., 2015; Driehuis et al., 2020). Briefly, surgical tumor pieces were minced into 1 mm fragments with a sterile scalpel and enzymatically digested with Accutase (Sigma-Aldrich, A6964) for 30 min at 37 °C on an orbital shaker. Cells were then embedded into 50 µL domes of Cultrex Reduced Growth Factor Basement Membrane Extract, Type 2, Pathclear (R&D Systems, 3533-001-02) into 24-well plates and covered with human complete medium (hCPLT, according to Boj et al. and Driehuis et al.) containing Advanced DMEM/F-12 (Gibco, 12634028), HEPES (Gibco, 15630-080), GlutaMAX (Gibco, 35050061), Primocin (Invivogen, ant-pm-2), WNT3A conditioned media, R-spondin1 conditioned media, B27 supplement (Gibco, 17504-001), Nicotinamide (Sigma-Aldrich, N0636), N-acetylcysteine (Sigma-Aldrich, A9165), mouse Noggin (Gibco, AF-250-38), human EGF (Gibco, AF100-15), human FGF (Gibco, AF-100-26), human Gastrin I (Tocris Bioscience, 3006), A 83-01 (Tocris Bioscience, 2939) and Y-27632 Rho Kinase inhibitor (Sigma-Aldrich, Y0503). Cultures were maintained at 37 °C in a humidified incubator with 5% CO_2. The culture medium was replaced regularly, and organoids were passaged for cell expansion approximately every 5 to 14 days depending on cell density and growth rate.

Drugs

In vitro cell viability assays were performed using the following compounds: Gemcitabine hydrochloride (Sigma, G6523), SN-38 (Cayman, 15632), 5-Fluorouracil (Cayman, 14416), Palbociclib (Cayman, 16273), Paclitaxel (Cayman, 10461), Oxaliplatin (Cayman, 13106), Trametinib (Cayman, 16292), RMC-7977 (MedChem Express, HY-156498), S63845 (Selleck Chem, S8383), Venetoclax (Selleck Chem, S8048), Navitoclax (Selleck Chem, S1001), A-1331852 (Selleck Chem, S7801). *In vivo* studies were performed using the following compounds: Gemcitabine hydrochloride (USP, 1288463).

Lentivirus and retrovirus production

Lentiviral transduction was used to generate CRISPR-mediated knockout cell lines, MCL-1 overexpressing cell lines, and Nuclight expressing cell lines. Lentivirus was produced using 3rd generation packaging systems. HEK293T cells cultured in DMEM/F12 medium with 10% FBS were transfected with 6 µg of the relevant transfer plasmid, 1.5 µg of pMD2.G (Addgene, 12259), 3 µg of pMDLg/pRRE (Addgene, 12251), and 1.5 µg of pRSV-REV (Addgene, 12253) using TransIT-LT1 transfection reagent (MirusBio, MIR 2304). Media was replaced after overnight transfection and harvested for viral particle collection after 48 hours. Collected virus was filtered though 45µm sterile syringe filters and stored at -80°C time of lentiviral transduction.
Ecotropic retrovirus was utilized for the generation of Omi-mCherry expressing cell lines. Retrovirus was generated by transfecting HEK293T with 5 µg the pBabe-Omi-mCherry transfer plasmid (Addgene, 48685) and 5 µg of pCL-Eco packaging plasmid (Addgene, 12371) using TransIT-LT1 transfection reagent (MirusBio, MIR 2304). Media was replaced after overnight transfection and harvested for viral particle collection after 48 hours. Collected virus was filtered though 45µm sterile syringe filters and stored at -80°C time of lentiviral transduction.

Production of Nuclight expressing cancer cell lines

Murine and human PDAC cell lines were engineered to stably express a nuclear-restricted red fluorescent protein (Nuclight; Sartorius, BA-04887) to facilitate live cell counting using the manufacturer's protocol. For mPDAC1-3 cell lines, CRISPR/Cas9 gene editing was utilized to knockout YFP expression. sgRNAs targeting YFP were designed and protospacer sequences targeting YFP were purchased as single strand oligonucleotides from IDT using standard desalting purification. Oligonucleotides were then cloned into the lentiCRISPRv2-Blast vector (Addgene, 83480) using previously published methods (Sanjana et al., 2014). mPDAC1-3 cells were lentivirally transduced with the resulting vectors as previously described (Apiz Saab et al., 2023). Transduced cells were selected over the course of 5 days with treatment of 5 µg/ml blasticidin and sorted using a BD FACSAria II Cell Sorter to isolate a polyclonal YFP-negative and Nuclight-positive mPDAC culture.

CRISPR vector cloning and CRISPR-mediated gene knock out in cell lines

CRISPR/Cas9 gene editing was utilized to generate knockout mPDAC cell lines for *Bcl2l1* and *Bax/Bak1*. The top 2 single guide RNAs (sgRNAs) from the Brie library (Doench et al., 2016) were selected to perturb *Bcl2l1*. Protospacer sequences targeting *Bcl2l1* or control non-targeting sequences purchased as single strand oligonucleotides from IDT using standard desalting purification. Oligonucleotides were then cloned into the lentiCRISPRv2-Blast vector (Addgene, 83480) using previously published methods (Sanjana et al., 2014). mPDAC1-TIFM cells were lentivirally transduced with the resulting vectors as previously described. Transduced cells were selected over the course of 5 days with treatment of 5 µg/ml blasticidin. Following selection, *Bcl2l1* knockout was confirmed by immunoblotting for BCL-XL. BCL-XL knockout proved highly efficient in mPDAC1 cells and therefore cell viability and immunoblotting assays were performed using this polyclonal cell population.

Dual targeting of *Bax/Bak1* was accomplished by cloning two small guide RNA and promoters into the lentiCRISPRv2 vector (Addgene, 52961) as previously described (Romero et al., 2020). The top sgRNAs

against *Bax* and *Bak1* were selected from the Brie library (Doench et al., 2016) and utilized to design dsDNA fragments (IDT) containing the first sgRNA (whose expression is driven by constitutive expression from the U6 promoter contained in the lentiCRISPRv2 vector backbone), H1 promoter (to drive constitutive expression of a second sgRNA) and the second sgRNA. The dsDNA fragment was flanked by BsmBI restriction sites to facilitate subcloning into lentiCRISPRv2. dsDNA fragments were then cloned into lentiCRISPRv2 as described above. mPDAC1-RPMI cells were lentivirally transduced with the above dual-targeting vectors (or control vectors containing two non-targeting sgRNAs). Single sgRNA knockout of *Bax/Bak1* proved inefficient in mPDAC1 cells. Work from other groups suggests that targeting two sgRNAs against a single gene can improve efficiency in CRISPR systems (Replogle et al., 2022). Therefore, we cloned additional *Bax/Bak1* dual targeting vectors into the lentiCRISPRv2-Blast vector (Addgene, 83480). We then transformed mPDAC1 cells with both lentiCRISPRv2-Blast and lentiCRISPRv2 vectors and selected cells using both blasticidin (5 µg/ml) and puromycin (2 µg/ml) over the course of 5 days. *Bax* and *Bak1* knockout was confirmed by immunoblotting and we observed high knockout efficiency using this approach. Cell viability assays were performed using this polyclonal cell population.

All sgRNA sequences used in this study are listed in the table below:

Gene ID	sgRNA	Protospacer Sequence
Bcl2l1	1	AGTAAACTGGGGTCGCATCG
Bcl2l1	2	CTGCTCAAAGCTCTGATACG
Bax	1	GACACGGACTCCCCCCGAGG
Bax	2	CTGATGGCAACTTCAACTGG
Bak1	1	GGTAGACGTACAGGGCCAGA
Bak1	2	GGAACTCTGTGTCGTAGCGC
YFP	1	CAACTACAAGACCCGCGCCG

Generation of Omi-mCherry expressing cell lines

mPDAC1 cells were transduced with retroviral particles to express Omi-mCherry (Addgene, 48685) and transduced cells were selected by treatment with 2 µg/ml puromycin over the course of 3 days. Following puromycin selection, cells were sorted via using a BD FACSAria II cell sorter to ensure uniform expression of the Omi-mCherry reporter in the mPDAC1 cells.

Generation of Mcl-1 overexpression cell lines

A dsDNA fragment encoding *Mcl1* cDNA (Twist Biosciences) was cloned into pLJM1-empty vector (Addgene, 91980) at the NheI restriction site via Gibson assembly. This vector enables constitutive expression of MCL-1 from the CMV promoter. Nuclight-expressing mPDAC4-TIFM cells were transduced with pLJM1-Mcl1 or empty pLJM1 lentivirus and selected for using 2 µg/ml puromycin over the course of 3 days.

IncuCyte cell viability and proliferation assays

For chemotherapy sensitivity assays, cells were plated in 96-well tissue culture plates at a density of 1500 cells/well and allowed to attach overnight. The following day, the media was removed from each well and replaced with fresh media containing Cytotox Green dye (Sartorius, 4633) at 50nM and the indicated concentration of compounds or vehicle. Plates were regularly scanned using a Sartorius/Essen BioScience IncuCyte S3 Instrument to monitor changes in cell viability and cell number over time. Unless otherwise indicated, all data shown reflects cell viability at 72 hours of the relevant treatment. Cellular segmentation and object quantification from the red and green fluorescence channels was performed using the IncuCyte analysis

software. Cell viability was quantified based on the proportion of red and green objects identified across the entire well, using the following formula: cell viability (%) = $(\frac{\#\,red\ objects}{\#\,red\ objects + \#green\ objects}) * 100$.

In some experiments, cell proliferation rates were determined in response to drug treatments. Here, cell proliferation rates were calculated as the number of population doublings per day, based on the change in the number of red objects from an initial timepoint and a final timepoint. These values were calculated according to the following population growth formula, $doublings\ per\ day = \left(\frac{1}{\#\ days}\right) * log_2(\frac{final\ cell\ count}{initial\ cell\ count})$.

Normalized growth rate inhibition (GR) analysis

GR_{toxic} estimates were determined for mPDAC1 cells treated with a titration of targeted and chemotherapy drugs using initial and final live/dead cell counts determined by IncuCyte-based live cell imaging experiments shown in Fig. 2C-F as previously described (Hafner et al., 2016) using the GRcalculator website, (grcalculator.org). GR_{max} estimates were similarly determined.

Propidium iodide-exclusion viability assay

Cell viability was assessed in certain experiments by propidium iodide staining coupled with flow cytometry, which also determines cell viability based on loss of plasma membrane integrity. mPDAC cells were plated in 6-well tissue culture dishes at a density of 100,000 cells per well and allowed to adhere overnight. The following day, the medium on each culture was changed and included compounds at indicated concentrations of vehicle. After indicated periods of drug treatment, propidium iodide (thermos P3566) was added to the culture medium at a concentration of 1.5 µg/ml and cultures were incubated at 37°C for 30 minutes to label dead cells. Afterwards, the medium was collected, and the dead cell fraction was isolated by centrifugation at 1000 x g for 5 minutes at 4 °C. Simultaneously, adherent cells were detached using 1% Trypsin-EDTA (Gibco 15400054) in serum-free RPMI-1640 for 20 minutes at 37 °C. The detached cell and floating cell fractions were combined and washed 3 times with PBS containing 1% BSA. Cells were strained with 40 µm cell strainers and analyzed by flow cytometry on a BD LSR Fortessa instrument. A minimum of 10,000 events per sample were captured for data analysis conducted using FlowJo software. Cells were gated based on the signal intensity of FSC-A and SSC-A channels. Singlets were then gated based on the intensity of FSC-H and SSC-A channels. Viable cells were then gated based on negative propidium iodide labeling, and thresholding for positive staining was determined based on the fluorescence intensity of an unlabeled cell sample.

Assessment of chemotherapeutic impact on patient-derived organoids

To test the impact of chemotherapeutics on patient-derived organoids derived in TIFM, TIFM-derived organoids were replated into two 35 uL UltiMatrix domes in a pre-warmed 24-well plate and cultured in one of two media: advanced DMEM/F12 or TIFM basal medium. After three days, organoids were replated as 10 µL UltiMatrix domes into a pre-warmed 48-well plate taking care to avoid air bubbles. For each medium, 1 mL of each media was prepared with five gemcitabine concentrations were prepared (0 nM, 10 nM, 100 nM, 1 µM, 10 µM). 250 µL of media was added to each well. Triplicate wells were prepared for each drug concentration in each medium. The 48-well plate was then incubated in a Sartorius/Essen BioScience IncuCyte S3 Instrument with the lid on and organoids were monitored using the Organoid QC Assay over four days. Organoid area from three randomly selected organoids per well was measured daily over 4 days using OrganoID software as previously described (Matthews et al., 2022).

To test the impact of chemotherapeutics on patient-derived organoids derived in standard medium that were cultured in either TIFM or standard media, organoids in standard organoid medium were dissociated into single cells by dissolving the domes for 2.5 hours at 37 °C with Collagenase/Dispase (Roche, 10269638001) and afterwards digested into single cells using Accutase (Sigma-Aldrich, A6964) for 30 min on an orbital shaker. Cells were then seeded into white bottom 96-well plates pre-coated with Cultrex Reduced Growth Factor

Basement Membrane Extract, Type 2, Pathclear (R&D Systems, 3533-001-02) diluted in 1:3 PBS (Gibco, 10010023), at a density of 2,000 cells per well in hCLPT medium or at 5,000 cells per well in TIFM. Twenty-four hours after seeding, cells were treated in triplicates with concentrations ranging from 0.013 to 50 μM of gemcitabine (Selleckchem, S1714). After 4 days of drug incubation, cell viability was analyzed using Cell Titer Glo 2.0 Assay (Promega, PRG9242) according to the manufacturer's protocol. Luminescence was measured for 1000 ms using a microplate reader (Varioskan LUX™, Thermo Scientific). Viability percentages were normalized to vehicle-treated cell viability.

MOMP reporter assay

Cells were plated in 12-well tissue culture plates at a density of 30,000 cells per well and allowed to attach overnight. Cells were then treated the following day with 125 nM Gemcitabine. After 48 hours, the supernatant was collected and centrifuged at 1000 x g for 5 minutes to pellet the floating cells. Simultaneously, cells still adherent to the plate were detached using 1% Trypsin-EDTA (Gibco, 15400054) in serum-free RPMI-1640 for 20 minutes at 37 °C. Detached cells in Trypsin-EDTA were combined with the floating cells and centrifuged at 1000 x g for 5 minutes. 300 nM DAPI (Thermo, D1306) was added to the resulting pellet and incubated on ice for 5 minutes to label dead cells. The cells were then washed once with PBS plus 1% BSA and resuspended in PBS. Cells were strained with 40 μm cell strainers and analyzed by flow cytometry on a BD LSR Fortessa instrument. A minimum of 10,000 events per sample were captured for data analysis conducted using FlowJo software. Cells were gated based on the signal intensity of FSC-A and SSC-A channels. Singlets were then gated based on the intensity of FSC-H and SSC-A channels. Viable cells were then gated based on negative DAPI labeling. Viable, post-MOMP cells were determined based on low red fluorescence from the Omi-mCherry reporter. Fluorescence intensity values from the Omi-mCherry reporter exhibited a bimodal distribution, and the threshold was chosen as the minimum between these two population peaks.

Immunoblotting

Cells were plated during log-phase of growth into 6-well plates at a density of 100,000 cells per well and allowed to adhere overnight. Cells were then washed with PBS and lysed on ice for 15 minutes using RIPA lysis and extraction buffer (Thermo, 89900) supplemented with Pierce protease inhibitor cocktail (Thermo A32963) and Pierce phosphatase inhibitor cocktail (Thermo, A32957). During drug treatment experiments that would result a loss of cell viability, floating cells in the medium were simultaneously isolated by centrifugation at 1000 x g for 5 minutes and added to the lysate of the adherent cells. Lysates were sonicated three times for 10 s using a probe sonicator. Insoluble fractions were then removed by centrifugation at 21,000 x g for 20 minutes at 4 °C. Protein concentration of lysates were determined by BCA assay (Thermo, 23225). Protein lysates (30–50 μg) were resolved on sodium dodecyl sulfate–poly-acrylamide gel electrophoresis (SDS-PAGE) 4–12% Bis-Tris Gels (Invitrogen, NP0321) by running at 85V for 2 hours and transferred to a polyvinylidene difluoride membrane using the iBlot 2 Dry Blotting System (Invitrogen, IB21001). Membranes were blocked with Intercept Blocking Buffer (LI-COR, 927-70001) at room temperature for 1 hour, and stained overnight at 4 °C with the following primary antibodies: BCL-XL (1:1000 dilution, Cell Signaling 2764S), BIM (1:750, Cell Signaling 2933S), BAX (1:750, Cell Signaling 14796S), BAK (1:750, Cell Signaling 12105), BCL2 (1:1000, Cell Signaling 3498), MCL1 (1:750, Cell Signaling 94296), Histone H2A.X (1:1000, Cell Signaling 7631S), phosho-H2A.X (Ser139) (1:1000, Cell Signaling 9718), ACTB (1:2000, Proteintech 66009-1-Ig), Cleaved CASP3 (Asp175) (1:1000, Cell Signaling 9661), COXIV (1:1000, Abcam, Ab16056), TUB1A (1:1000, Cell Signaling 3873T), MAPK3/MAPK1 (Erk1/2) (1:1000, Cell Signaling 4695), Phospho- MAPK3/MAPK1 (Erk1/2) (Thr202/Tyr204) (1:1000, Cell Signaling 9101). Membranes were washed 3 x 5 minutes with PBS-T buffer and stained with the following secondary antibodies for 1-2 hours at room temperature: IRDye 680LT Goat anti-Rabbit IgG (1:10,000 dilution, Licor 926-68020), IRDye 800CW Goat anti-Mouse IgG (1:10,000, Licor 926-32210). Fluorescent membranes were scanned using a Licor Odyssey CLX instrument. Approximate molecular weights of identified protein species were determined by comparison to migration of the Chameleon duo pre-stained protein ladder (Licor, 928-60000).

Co-immunoprecipitation assays

For co-immunoprecipitation assays, 1,000,000 mPDAC1 TIFM and RPMI cells were seeded per condition in 10cm plates and allowed to adhere overnight. The following day, cells were treated with vehicle (DMSO), 125 nM Gemcitabine, or 125 nM Gemcitabine plus 100 nM A-1331852. After 24 hours of treatment, media was collected and floating cells were pelleted by centrifuging at 1000 x g for 5 minutes. Adherent cells were washed with 2 mL PBS and lysed using complete Co-IP lysis buffer (0.2% NP-40, 50 mM Tris-HCL, 150 mM NaCl, 1 mM EDTA, and 10% glycerol at pH 7.5 and supplemented with Pierce protease inhibitor cocktail (Thermo, A32955) and Pierce phosphatase inhibitor cocktail (Thermo, A32957)) and incubated on ice for 15 minutes. Lysates from adherent and floating fractions were combined and the insoluble fraction was removed by centrifugation at 21,000 x g for 20 minutes at 4°C. Protein concentrations of lysate were determined by BCA assay (Thermo, 23225) and 1 mg total protein lysate was used as input for co-immunoprecipitation reactions. Samples were initially pre-cleared with Protein A/G Agarose beads (Santa Cruz, sc-2003), rotating for 1hr at 4 °C. 1 µg of BCL-XL IgG antibody (Cell Signaling 2764) or 1µg of Rabbit IgG Isotype Control (Cell Signaling 3900) was added to lysates, which were then rotated overnight at 4°C.

The following day, 20 µl of Protein A/G Agarose beads were added to lysates to capture antibody:protein complexes and rotated for 3 hours at 4°C. Agarose beads were pelleted by centrifugation at 1000 x g for 3 minutes at 4 °C and the supernatant removed. Samples were washed 3x with complete Co-IP lysis buffer and eluted using complete Co-IP lysis buffer plus 1x SDS-PAGE sample loading buffer (Thermo J61337AD) by boiling samples at 100 °C for 5 minutes. Samples were run on 4-12% Bis-Tris Gels and transferred as described above. Membranes were blocked with Intercept Blocking Buffer (LI-COR, 927-70001) at room temperature for one hour and incubated overnight with the primary antibodies listed above. Membranes were then washed 3 x for 5 minutes with PBS-T and then incubated with Mouse Anti-rabbit Conformation Specific IgG (1:2000 dilution, Cell Signaling 3678) for one hour at room temperature. Membranes were washed 3 x for 5 minutes with PBS-T and then incubated with Anti-mouse IgG, HRP-linked Antibody (1:1000 dilution, Cell Signaling 7076) for one hour at room temperature. Membranes were treated with SuperSignal™ West Dura reagent (Thermofisher, 34075) for 2 minutes and then chemiluminescence was imaged using an Invitrogen iBright FL1000 digital imager. The molecular weights of protein bands were determined based on migration relative to visible marker bands in Chameleon duo pre-stained protein ladder (Licor, 928-60000).

Subcellular fractionation

20,000,000 mPDAC1 TIFM and RPMI cells were plated in 15 cm dishes and allowed to adhere overnight. The following day, cells were treated with 250 nM gemcitabine and harvested at the following time points: 0 hr, 12 hr, and 24 hr. Subcellular fractionation was performed using the mitochondrial isolation kit for cultured cells (Thermo, 89874) using the dounce homogenization method. Protein concentrations from cytosolic and crude mitochondrial lysate fractions were measured by BCA assay (Thermo, 23225). Samples were then run on 4-12% Bis-Tris Gels and transferred as described above. Membranes were subjected to fluorescence-based immunoblotting using COXIV, BAX, and TUBA1A primary antibodies as described above.

Alkaline comet assays

Alkaline comet assays were performed using the Trevigen CometAssay kit (Bio-Techne 4250-050-K). mPDAC1 RPMI and TIFM cells were plated in 6-well tissue culture plates at a density of 200,000 cells per well and allowed to adhere overnight. The following day, cells were treated with chemotherapeutics (vehicle, 150 nM gemcitabine, 10 µM SN-38 or 5µM 5-FU) and harvested after 18 hours of treatment. Adherent cells were washed once with PBS and detached using 1% Trypsin-EDTA (Gibco 15400054) in serum-free RPMI-1640 for 20 minutes at 37 °C. Resuspended cells are diluted in PBS, added to 37 °C molten low melt agarose, and spread over pre-coated CometAssay slides. Slides are placed in 4 °C to solidify the agarose for 30 minutes and placed in pre-chilled 4 °C CometAssay lysis buffer to lyse overnight. The following day, slides are placed in pre-chilled alkaline unwinding solution for 1 hour at 4 °C. Slides are then subjected to electrophoresis in

chilled alkaline unwinding solution at 4 °C using 25 V for 35 minutes. Slides are rinsed twice with water for 5 minutes, once with 70% ethanol for 5 minutes and dried at 37 °C for 15 minutes. Slides are then stained with SYBR green (Thermo, S33102) diluted 1:10,000 in TE buffer (10 mM Tris-HCL pH 7.5, 1 mM EDTA) for 30 minutes. Slides are rinsed twice with water and stored at room temperature until analysis performed the following day. Widefield imaging of comet assay slides was performed using an Olympus IX81 inverted widefield microscope with a 20x objective capturing fluorescence signal with 480/40 nm excitation and 510 nm emission settings. A minimum of 100 cells per sample were imaged for each experiment. Images were analyzed in Fiji/ImageJ software using the OpenComet plugin (Gyori et al., 2014). Comet finding was performed using background correction and the brightest region head finding approach. Valid comet finding was manually confirmed for each data point included in the analysis.

Cell cycle analysis

Cell cycle profiles were determined using the Click-iT EdU Flow cytometry kit (Thermo, C10424). Given the presence of unlabeled nucleosides in TIFM medium that may interfere with analysis of EdU incorporation, a minimal TIFM medium containing only the pools of metabolites comprising glucose, vitamins and amino acids was generated for use during the labeling period. mPDAC1 RPMI and TIFM cells were plated in 6-well tissue culture plates at a density of 200,000 cells per well and allowed to adhere overnight. The following day, relevant treatment conditions were applied and harvested at the following timepoints: 0 hr, 24 hr, and 48 hrs. Prior to sample collection, cells were rinsed once with PBS and pulsed with 10 μM EdU in RPMI or minimal TIFM medium for 45 minutes at 37 °C. Cells were then rinsed with PBS and detached using 1% Trypsin-EDTA (Gibco 15400054) in serum-free RPMI-1640 for 20 minutes at 37 °C. Samples were then fixed for 15 minutes at room temperature with Click-iT fixative reagent and permeabilized with the Click-iT saponin-based permeabilization and wash reagent for 15 minutes at room temperature. Click-iT reactions with Alexa Fluor 647 azide were performed for 30 minutes at room temperature and cells were then stained with 300nM DAPI (Thermo, D1306) for 15 minutes prior to analysis. Flow cytometry analysis was performed using a BD LSR Fortessa Instrument. Cells were gated based on the signal intensity of FSC-A and SSC-A channels. Singlets were then gated based on the intensity of FSC-H and SSC-A channels. Total DNA content was determined based on fluorescence intensity from the DAPI channel. Active DNA replication was determined based on fluorescence intensity from the AF647 channel. Cell cycle profiles of samples were determined using FlowJo analysis software. The population of cells in G1-phase was determined as the event population with low DAPI signal and low EdU signal, cells in G2/M-phase as the event population with high DAPI signal and low EdU signal, and cells in S-phase with intermediate DAPI and high EdU signal. Proportions were determined based on the sum of events from these 3 populations.

BH3 profiling assay

We performed BH3 priming as described previously (Ryan and Letai, 2013). Briefly, BH3 priming treatment plates were prepared in black 384-well plates containing 15 μL volume of MEB buffer (150mM D-Mannitol, 10mM HEPES pH 7.5, 50mM KCl, 5mM Succinate, 20μM EGTA, 20μM EDTA, 0.1% BSA) containing the indicated concentration of BIM peptide (Genscript), 2 μM JC-1 (Invitrogen, T3168), 100 μg/mL digitonin, 20 μg/mL oligomycin and 10 mM 2-mercaptoethanol. Detached mPDAC cell samples were resuspended in MEB buffer at 20,000 cells per 15 μL. 15 μL of mPDAC cells in MEB were transferred to each well in the 384-well plate for a total volume of 30 μL per well. The treatment plate was immediately loaded onto a pre-heated fluorescence plate reader (SpectraMax iD5 Multi-Mode Microplate Reader, Molecular Devices) set to 30 °C. Fluorescence of JC-1 was monitored using an excitation of 545nm and emission of 590nm. Relative fluorescence intensity was recorded every 5 minutes for 180 minutes. The percentage of mitochondrial membrane depolarization was determined based on the area under the curve (AUC) estimates for each sample well relative to the positive (FCCP, carbonyl cyanide-p-trifluoromethoxyphenylhydrazone) and negative (PUMA2A, a modified BH3-only peptide without MOMP-inducing activity obtained from Genscript) depolarization controls, using the following formula: $\% \, Depolarization = \left(1 - \frac{Sample_{AUC} - FCCP_{AUC}}{PUMA2A_{AUC} - FCCP_{AUC}}\right) * 100.$

Animal experiments

Animal experiments were approved by the University of Chicago Institutional Animal Care and Use Committee (IACUC, Protocol #72587) and performed in strict accordance with the Guide for the Care and Use of Laboratory Animals of the National Institutes of Health. Mice were housed in a pathogen-free animal facility at the University of Chicago with a 12 hour light / 12 hour dark cycle. Humidity is maintained between 30–70% humidity and temperature is maintained at 68–74 °F in the facility.

Generation of orthotopic allograft PDAC tumors

Female C57BL6J mice 8–12 weeks of age were obtained from Jackson Laboratories (Strain #000664). mPDAC3-RPMI cells were resuspended in sterile serum-free RPMI and Reduced Growth Factor Basement Membrane Extract (R&D Biosystems, 3433-010-01) at a final concentration of 5.6 mg/ml. To generate orthotopic tumors, 100,000 cells were injected as a 20μL Reduced Growth Factor Basement Membrane Extract:PDAC cell mixture into the splenic lobe of the pancreas of anesthetized mice as previously described (Erstad et al., 2018). Following implantation, mice were regularly monitored for changes in behavior, body weight, and tumor presence by abdominal palpation.

In vivo gemcitabine treatment

Orthotopic allograft tumors were established with mPDAC3-RPMI cells as described above. 2 weeks after tumor implantation, gemcitabine treatment was initiated. Gemcitabine hydrochloride (USP, 1288463) was resuspended in PBS, sterilized by syringe filtration, and dosed at 120 mg/kg via intraperitoneal injection. Tumor-bearing mice received gemcitabine or PBS injections twice weekly for 3 weeks. Mice were euthanized 24 hours after the final treatment with gemcitabine. Tumor weights were measured, and samples were fixed in formalin overnight and embedded in paraffin.

Immunofluorescence analysis of tumor sections

Tumor sections were deparaffinized and rehydrated with xylenes and serial 1224 dilutions of ethanol to deionized water. Sections were then incubated in antigen retrieval buffer (Agilent Dako, S1699) and heated in a steamer at 97 °C for 20 minutes. Primary antibodies for anti-phospho-H2A.X (Ser139) (1:50 dilution, Cell Signaling 9718) or anti-Cleaved Caspase-3 (Asp175) (1:50 dilution, Cell Signaling 9661) were applied on tissue sections at 4 °C overnight. Tissue sections were washed with Tris buffered saline and then secondary antibody, goat anti-rabbit IgG Alexa Fluor 594 (1:200 dilution, Thermo A-11012), was applied for 1 hour at room temperature. Coverslips were mounted on slides using Prolong Gold Anti-fade Mountant with DAPI (Thermo, P36931). Slides were imaged using an Olympus VS200 Slideview Scanner with a 20x objective. DAPI fluorescence intensity was captured using 378/52 excitation and 432/36 emission filter. AF594 fluorescence intensity was captured using 578/21 excitation and 641/75 emission filter. Analysis of phospho-H2AX and cleaved caspase-3 positivity in tumors was performed using QuPath (Bankhead et al., 2017). Regions of interest across the tumor body, excluding nectrotic core regions, were manually drawn for each tumor section. Positively labeled cells for phospho-H2AX or cleaved caspase-3 were determined using the positive cell detection function, using DAPI label to facilitate total cell detection. A thresholding cutoff for positive cells was determined based on the mean pixel intensity for a sample of positive cells identified from a representative tumor image.

Tumor adapted culture generation

Orthotopic allograft tumors were established with mPDAC3-RPMI cells as described above. 4-6 weeks after implantation, tumors were processed for cancer cell isolation. 4 tumors were pooled as a single sample and dissociated as described previously (Apiz Saab et al., 2023). Single cell tumor suspensions were plated onto

10 cm tissue culture plates in RPMI-1640 medium with 10% dialyzed FBS supplemented with penicillin-streptomycin (ThermoFisher, 15140-148) and gentamicin (ThermoFisher, 15750060). The tumor cell suspension was then allowed to adhere and acclimate to standard culture conditions for 48 hours. To isolate cancer cells from the total tumor cell population, tumor cells were detached using 1% Trypsin-EDTA (Gibco, 15400054) in serum-free RPMI-1640 for 20 minutes at 37°C. Samples were then blocked using 10% normal mouse serum (Thermo, 10410) in PBS containing 1% BSA. Samples were then stained with rat anti-mesothelin (mouse) (MBL, D233-3) antibody at 1:100 dilution in 10% normal mouse serum in PBS containing 1% BSA for 30 minutes at 4 °C. Samples were washed twice with PBS containing 1% BSA and then stained with APC-conjugated goat anti-rat IgG (Thermo, A10540) secondary antibody at 1:200 dilution in 10% normal mouse serum in PBS containing 1% BSA for 20 minutes at 4 °C. APC-positive cancer cells were sorted via FACS using a BD FACSAria II Cell Sorter and returned to standard culture conditions supplemented with penicillin-streptomycin and gentamicin pen/strep and gentamicin for 48 hours. After 48hrs, sorted tumor-adapted cells were replated for subsequent analyses.

RNA-sequencing and analysis

mPDAC1 RPMI and TIFM cultured cells were plated at 50,000 cells per well in 6 cm dishes overnight. The following day, cells were treated with vehicle or 125 nM gemcitabine. After 24 hours of treatment, RNA was extracted from treated cells using the RNeasy Micro Kit (Qiagen, 74004). RNA quality and quantity were then assessed using the 2100 Bioanalyzer System (Agilent).

Library preparation and sequencing

Strand-specific RNA-SEQ libraries were prepared using the TruSEQ mRNA RNA-SEQ library protocol (Illumina). Library quality and quantity were assessed using the Agilent bio-analyzer and libraries were sequenced using an Illumina NovaSEQ6000 platform at the University of Chicago Functional Genomics Facility (RRID:SCR_019196).

RNA sequencing data analysis

Data processing and analysis were done using the R-based Galaxy platform (https://usegalaxy.org/). Quality control was performed prior and after concatenation of the raw data with the MultiQC and FastQC tools, respectively. All samples passed the quality check with most showing ~20% sequence duplication, sequence alignment greater or equal to 80%, below and below 50% GC coverage. Samples were aligned and counts were generated using HISAT2 (Galaxy Version 2.2.1+galaxy0, NCBI genome build GRCm38/mm10) and featureCounts (Galaxy Version 2.0.1+galaxy1), respectively. Differential expression analyses were performed with limma (Galaxy Version 3.48.0+galaxy1). Gene set enrichment analyses (GSEA) were performed in RStudio with the clusterProfiler package (Wu et al., 2021) using the GSEA function with C2 curated gene sets from MsigDB and Benjamini-Hochberg multiple tests correction. Altered gene set enrichments were determined for mPDAC1-RPMI cells by initially separating gene set enrichments into positive and negatively enriched gene sets, sorting by the lowest adjusted p-value, and then sorting by the highest normalized enrichment score. The top ten positive and negatively enriched gene sets with adjusted p-values less than 0.05 were selected, and the enrichment scores for this subset was then determined for gemcitabine regulated genes in mPDAC1-TIFM cultures.

Transcription factor activity inference for mPDAC1 RPMI and TIFM differential gene expression datasets was performed using the decoupleR package (Badia-I-Mompel et al., 2022). Analysis was performed using a univariate linear model (ULM) for predicted TF activity based on known TF-gene interactions and observed differential gene expression with the run_ulm() function. The murine CollecTRI gene regulatory network was used as input for the known TF-gene interactions. Transcription factors with predicted enhanced activity were determined based on the highest ULM enrichment score.

Clonetracr analysis

The ClonTracer library was obtained from Addgene (67267). 50,000 mPDAC3 cells in RPMI-1640 supplemented with 10% dialyzed FBS were barcoded by lentiviral infection at an MOI of 0.1 to ensure infection of 5,000 cells with one unique barcode each. Cells were then allowed to expand for 8 population doublings before selection with 2 µg/ml puromycin over the course of 3 days. After selection, cells were maintained at a coverage of 85 cells per guide. Barcode-expressing cells cultured in RPMI-1640 were transferred into RPMI (RPMI → RPMI) or gradually transitioned into TIFM (RPMI → TIFM) over a period of 17 population doublings. Cells in each condition were split at 90% confluency and refed every day with fresh media to avoid nutrient depletion. For transitioning cells into TIFM, cells were initially plated in 90% TIFM/10% RPMI until they reached confluency. Cells were then transitioned into 99% RPMI/1% TIFM until they reached confluency. Cells were then transferred into 100% TIFM and maintained under these conditions until 17 doublings were completed (PD17). PD17 for both conditions, as well as the day 0 control (PD0), were frozen for later analysis. Genomic DNA was isolated from frozen cell pellets using the NucleoSpin BloodXL kit (Machery-Nagel, 740950). PCR was used to amplify the barcode region along with introducing Illumina adapters with 5 bp-long index sequences to each sample as previously described (Bhang et al., 2015). 1.6 µg genomic DNA was used as input for each PCR reaction, with each sample having two reactions to ensure sufficient template coverage. PCR products were column purified (Qiagen, 28104) and sequenced on an Illumina NovaSeqX NGS sequencing platform at the University of Chicago Functional Genomics Facility (RRID:SCR_019196). Quality control and filtering by hamming distance to account for sequencing errors was performed as described previously (Bhang et al., 2015). Briefly, FASTQ files were prepared and sequencing reads were filtered based on an average Phred quality score greater than 30. Barcodes differing by 1 base pair from a more abundant sequence occurring at less than 12.5% of its count, or 2 base pairs from a more abundant sequence occurring at less than 2.5% of its count, were reassigned to the more abundant barcode. Finally, only barcodes with at least two observations were included in the final dataset. Gini index was calculated using the ineq package in R. Histograms of barcode frequency were created using the top 2,500 barcodes in each condition. The relation in fitness between clones under RPMI → RPMI and RPMI → TIFM conditions was determined by initially calculating barcode abundance as the proportion of reads belonging to a unique barcode relative to the total reads within a sample. The log 2 fold change in the abundance of each barcode between PD0 and PD17 was then calculated for both medium conditions. Lastly, the spearman's rank correlation was calculated between the change in abundance of a clone under RPMI → RPMI and RPMI → TIFM conditions.

Data availability

Gene expression data associated with Fig. 3 is deposited in GEO with the accession code GSE306515.

Acknowledgements

We thank all members of the Muir lab, Benjamin Stanger and Yogev Sela for feedback and discussions on this project. We thank the University of Chicago Animal Resources Center (RRID:SCR_021806), especially Ani Solanki, for their assistance with animal models of pancreatic cancer. We thank the University of Chicago Genomics Facility (RRID:SCR_019196), Human Tissue Resource Center (RRID:SCR_019199), and Integrated Light Microscopy Core (RRID: SCR_019197) for experimental assistance. This work was supported by funding from the Ludwig Center for Metastasis Research, the University of Chicago Comprehensive Cancer Center, the National Cancer Institute (R01 CA276461) and the V Foundation (V Scholar Award) provided to A.M. C.J.H. acknowledges support from the National Cancer Institute (R37 CA283575) and the Sky Foundation. C.S.S. was supported by the National Cancer Institute (T32 CA009594 and F31 CA278362). G.C. was supported by the Pancreatic Cancer Action Network (Pancreatic Cancer Action Network Fellowship, funded by the Francois Wallace Monahan Fund). D.A. and P.B.J. were supported by the National Cancer Institute (T32 CA009594).

Ethics

Animal experiments were approved by the University of Chicago Institutional Animal Care and Use Committee (IACUC, Protocol #72587) and performed in strict accordance with the Guide for the Care and Use of Laboratory Animals of the National Institutes of Health. Human PDAC samples were obtained under approval by the Institutional Review Boards at the University of Chicago (20-1683).

Figure legends

Figure 1: The tumor microenvironment imprints chemotherapy resistance in PDAC cells. (A) Diagram of workflow for the comparison of chemotherapeutic killing of mPDAC cell lines derived from genetically engineered mouse models of PDAC into standard culture conditions and orthotopic murine PDAC tumors derived from the same cell lines. **(B)** Viability of mPDAC3-RPMI cells measured by IncuCyte cell viability assay after treatment with indicated concentrations of gemcitabine for 72 hours (n = 3). **(C)** mPDAC3-RPMI orthotopic tumor weights from animals treated with vehicle (n = 6) or gemcitabine (n = 8). **(D)** Experimental schematic for the comparison of chemotherapeutic sensitivity of cultured mPDAC3-RPMI cells that were kept in culture or were grown as orthotopic allografts in mice and then sorted from tumors and returned to culture for indicated periods of time (tumor-adapted). **(E-F)** Viability of mPDAC3-RPMI cells measured by propidium iodide exclusion. mPDAC3-RPMI cells were kept in culture or tumor-adapted and then returned to culture as shown in **(D)** and treated with the indicated concentrations of **(E)** gemcitabine (n = 3) or **(F)** SN-38 for 72 hours (n = 3). Statistical significance in C was assessed using the Mann-Whitney U test. For E and F, the area under the curve (AUC) was calculated and unpaired t-test was performed to determine significance in the difference of the AUC for the indicated cultures. *** $p \leq 0.001$ and **** $p \leq 0.0001$.

Figure 2: Tumor nutrient conditions are sufficient to imprint therapy resistance in PDAC. (A) Diagram of the generation of paired PDAC cell lines from murine PDAC tumors in TIFM or in RPMI. **(B)** Representative images of mPDAC1-TIFM and mPDAC1-RPMI cells expressing Nuclight incubated with Cytotox Green Dye and treated with 19 nM gemcitabine or vehicle for 72 hours. **(C-F)** Viability of indicated mPDAC-TIFM and mPDAC-RPMI cultures measured by IncuCyte cell viability assay treated with the indicated concentration of **(C)** gemcitabine (n = 3), **(D)** 5-fluorouracil (n = 3), **(E)** SN-38 (n = 3) or **(F)** RMC-7977 (n = 3) for 72 hours. **(G)** Diagram of experiment moving mPDAC1-TIFM cultures to RPMI medium (TIFM → RPMI) for various period of time and assessing chemotherapeutic response of these cultures. **(H)** Viability of mPDAC1-TIFM, mPDAC1-RPMI and mPDAC1-TIFM→RPMI cells measured by IncuCyte cell viability assays after the indicated time point in culture and treated with the indicated concentration of gemcitabine (n = 3) for 72 hours. **(I)** Diagram of the protocol for transitioning mPDAC-RPMI and human PDAC cell lines and organoids to grow in TIFM. We term these mPDAC-RPMI→TIFM cultures. **(J)** Viability of mPDAC1-RPMI and mPDAC1-RPMI→TIFM cultures measured by IncuCyte cell viability assay when treated with the indicated concentration of gemcitabine (n = 3) for 72 hours. **(K)** Viability of patient derived organoids measured by CellTiter-Glo assay in standard organoid culture media or TIFM following treatment with the indicated concentration of gemcitabine (n = 3) for 72 hours. Viability of indicated human PDAC cell lines measured by IncuCyte cell viability assay cultured in RPMI or TIFM when treated with the indicated concentration of **(L)** gemcitabine (n = 3), **(M)** 5-fluorouracil (n = 3) or **(N)** SN-38 (n = 3) for 72 hours. For C-F and J-N, the area under the curve (AUC) was calculated and unpaired t-test was performed to determine significance in the difference of the AUC for the indicated cultures. *** $p \leq 0.001$ and **** $p \leq 0.0001$.

Figure 3: TME nutrient stress induces chemotolerance by suppressing apoptotic priming
(A) (Left) Immunoblot confirmation of *Bax* and *Bak1* double knockout (*Bax/Bak1* DKO) in mPDAC1-RPMI cells. (Right) Cell viability measured by IncuCyte cell viability assay of mPDAC1-RPMI NTC and *Bax/Bak1* DKO cultures treated with the indicated concentration of gemcitabine (n = 3) for 72 hours. **(B)** Diagram of cell death by chemotherapy. Initial chemotherapeutic response requires exposure mediated by cellular transporters and damage from on-target activity such as DNA double stranded breaks, indicated by the presence of γH2AX.

Following cellular damage, a pro-death cellular response is generated, which may feature the upregulated expression of pro-apoptotic BH3-only proteins. A sufficiently strong death signal, in the case of apoptotic cell death, results in mitochondrial outer membrane permeabilization (MOMP). This event results in a commitment to cell death leading to cellular disassembly mediated by the activation of executioner caspases, which finally leads to loss of plasma membrane integrity. **(C)** (Right) Alkaline comet assay of mPDAC1-RPMI and mPDAC1-TIFM cultures treated for 18hrs with 150nM Gemcitabine (RPMI n = 58, TIFM n = 64) or DMSO vehicle (RPMI n = 61, TIFM n = 52). (Left) Representative images of comets following treatment with gemcitabine or vehicle. **(D)** Heatmap of C2 MSigDB gene sets with differential enrichment from GSEA analysis of mPDAC1 RPMI cultures treated for 24 hours with 125nM Gemcitabine versus DMSO vehicle control. All gene sets displayed a statistically significant enrichment of less than 0.05 after p-value adjustment by Benjamini-Hochberg correction. Right column displaying enrichment scores for the corresponding gene set following GSEA analysis of mPDAC1 TIFM cultures treated with gemcitabine under identical conditions. Values in heatmap displayed reflect normalized enrichment score (NES). **(E)** ULM enrichment scores predicting enhanced transcription factor activity for the top 5 differentially enriched TFs in mPDAC1-RPMI cells in response to gemcitabine treatment, with the enrichment scores for mPDAC1-TIFM cells displayed in parallel. **(F)** Immunoblots for γH2AX, BIM, and Cleaved Caspase-3 in mPDAC1-RPMI and mPDAC1-TIFM cells treated with 150nM Gemcitabine over time at the indicated timepoints. **(G)** Red fluorescence intensity of Omi-mCherry reporter expressing mPDAC1-RPMI and mPDAC1-TIFM cells treated with either gemcitabine or vehicle. **(H)** Percent of Omi-mCherry low cells (post-MOMP) in mPDAC cells cultured under the indicated medium and drug treatment conditions (n = 4). **(I)** Immunoblots for BAX in mitochondrial and cytosolic isolates from mPDAC1-RPMI and mPDAC1-TIFM cells treated with 250 nM gemcitabine over time at the indicated timepoints. **(J)** Relative mitochondrial depolarization of mPDAC1-RPMI and mPDAC1-TIFM cells in response to treatment with recombinant BIM peptide at the indicated concentrations (n = 3). **(K)** Immunoblots for BCL2 family members in the indicated mPDAC cell line and culture condition. **(L)** Immunoblots for BCL-XL, MCL-1, BIM and BAX following immunoprecipitation of BCL-XL or MCL-1 in mPDAC1-RPMI cell lysates. “Iso” sample reflects pulldown with isotype control rabbit IgG antibody. **(M)** Immunoblots for BCL-XL and BAX following immunoprecipitation for BCL-XL in mPDAC1-TIFM or mPDAC1-RPMI cell lysates following treatment with gemcitabine (125 nM) and A1331852 (100nM) as indicated for 24 hours. **(N)** Cell viability of mPDAC1-TIFM cells measured by IncuCyte cell viability assay following treatment with the indicated compounds for 72 hours (Gemcitabine, 150 nM), (A1331852 1 μM), (S63845 1 μM), (Venetoclax 1 μM), (Navitoclax 1 μM). Individual datapoints reflect the mean viability of 3 replicates for a single cell line (mPDAC1-4), as indicated in the figure legend (n = 4 cell lines). **(O)** (Left) Immunoblot confirmation of *Bcl-xL* knockout in mPDAC1-TIFM cells. (Right) Cell viability of *Bcl-xL* knockout or NTC mPDAC1-TIFM cells measured by IncuCyte cell viability assay, following treatment with the indicated concentrations of gemcitabine for 72 hours (n = 3). **(P)** Immunoblots for γH2AX, BIM, and Cleaved Caspase-3 in *Bcl-xL* knockout or NTC mPDAC1-TIFM cells following treatment with 150 nM Gemcitabine at the indicated timepoints. For A,J,O, the area under the curve (AUC) was calculated and unpaired t-test was performed to determine significance of differences in AUC for the indicated cultures. For C, H, N, unpaired t-tests were performed to determine significance of differences between sample conditions. For E, all gene sets displayed for the mPDAC1-RPMI sample had significant enrichment with a p-value of less than p=0.05 after multiple tests correction. For J, all transcription factors displayed had significant enrichment with a p-value of less than p=0.0001 after multiple tests correction. * p≤0.05, ** p≤0.01, and **** p≤0.0001.

Figure 4: The TME imprints a chemotolerant phenotype on PDAC cells. (A) Diagram of the generation of orthotopic allograft murine PDAC tumors from mPDAC3-RPMI cells and assessing chemotherapy tolerance by immunofluorescence analysis of cell death and DNA damage markers after gemcitabine treatment. **(B)** Representative immunofluorescence images of γH2AX and cleaved caspase-3 in vehicle and gemcitabine treated mPDAC3-RPMI orthotopic allograft tumors. Scalebar indicates 250 μm. **(C,D)** Quantification of PDAC cells staining positive for **(C)** γH2AX and **(D)** Cleaved Caspase-3 in vehicle (n = 6) and gemcitabine (n = 8) treated mPDAC3-RPMI orthotopic allograft tumors. **(E)** Diagram of workflow for the comparison of apoptotic priming of mPDAC cell lines adapted to growth in orthotopic allograft tumor conditions and returned to standard culture versus maintained in standard culture conditions. **(F,G)** Relative mitochondrial depolarization following

treatment with the indicated concentration of BIM peptide for mPDAC3-RPMI cells, which were tumor-adapted and returned to standard culture conditions for **(F)** 4 days or 4 weeks **(G)** or maintained continuously in standard culture (n = 3). For F,G, the area under the curve (AUC) was calculated and unpaired t-tests were performed to determine significance in the difference of the AUC for the indicated cultures. Statistical significance in C,D was assessed using the Mann-Whitney U test. * p≤0.05 and **** p≤0.0001.

Figure 2 - Figure supplement 1: Tumor nutrient conditions renders PDAC cells insensitive to a variety of chemotherapeutic and target therapies. (A-C) Viability of mPDAC1-TIFM and mPDAC1-RPMI cultures measured by IncuCyte cell viability assay treated with the indicated concentration of **(A)** paclitaxel (n = 3), **(B)** oxaliplatin (n = 3) or **(C)** trametinib (n = 3) for 72 hours. **(D)** Measurement relative organoid size of TIFM- and standard media-cultured patient-derived organoids over time following treatment with vehicle (TIFM n = 9, DMEM/F12 n = 6) and gemcitabine (100 nM) (TIFM n = 9, DMEM/F12 n = 6) for 72hrs. For A-D, the area under the curve (AUC) was calculated and unpaired t-test was performed to determine significance in the difference of the AUC for the indicated cultures. *** p≤0.001 and **** p≤0.0001.

Figure 2 - Figure supplement 2: Differences in growth rate do not account for differential sensitivity of mPDAC-RPMI and mPDAC-TIFM cultures to chemotherapy treatment. (A) Percentages of mPDAC1-TIFM and mPDAC1-RPMI cultures in G1, S and G2/M phases of the cell cycle (n = 3). **(B-E)** GR_{toxic} estimates for the indicated mPDAC-TIFM and mPDAC-RPMI cell line following treatment with the indicated concentration of **(B)** gemcitabine (n = 3), **(C)** 5-fluorouracil (n = 3), **(D)** SN-38 (n = 3), and **(E)** RMC-7977 (n = 3) for 72 hours. **(F)** GR_{max} estimates for the indicated mPDAC cell lines, culture condition and drug treatment (n = 3 cell lines). **(G)** Percentages of mPDAC1-TIFM cells treated with 100 nM gemcitabine for the indicated time periods in G1, S and G2/M phases of the cell cycle (n = 3). **(H)** Growth rates of vehicle treated mPDAC1-TIFM and mPDAC1-RPMI cultures and mPDAC1-RPMI cultures treated with 2.5 μM palbociclib (n = 3). **(I)** Viability of mPDAC1-TIFM and mPDAC1-RPMI cultures and mPDAC1-RPMI cells treated with 2.5 μM palbociclib cultures measured by IncuCyte cell viability assay following treatment with the indicated concentration of gemcitabine (n = 3) for 72 hours. For A, unpaired t-tests were performed to assess significance in differences in cell cycle phase between culture conditions. For F, paired t-tests were performed to assess significance in differences in GR_{max} estimates. For G, unpaired t-tests were performed to assess significance in differences in cell cycle phase between the indicated timepoint of gemcitabine treatment and the initial population. For H, unpaired t-tests were performed to assess significance in differences in proliferation rate. For I, the area under the curve (AUC) was calculated and unpaired t-tests were performed to determine significance in the difference of the AUC for the indicated cultures. * p≤0.05, *** p≤0.001 and **** p≤0.0001.

Figure 2 - Figure supplement 3: TIFM-cultured PDAC cells are quiescent during chemotherapy treatment but can resume proliferation upon drug removal. (A) Growth rates of mPDAC1-RPMI and mPDAC1-TIFM cultures measured every 6 hours over 2 days following exposure to 100 nM gemcitabine for 24 hours (n = 3). For A, the area under the curve (AUC) was calculated and unpaired t-test was performed to determine significance in the difference of the AUC for the indicated cultures. **** p≤0.0001.

Figure 2 - Figure supplement 4: Transitioning mPDAC-RPMI to grow in TIFM does not select for rare clonal populations. (A) Diagram of the lentiviral barcoding of mPDAC3-RPMI cells prior to transitioning these cells into TIFM as shown in Fig. 2I or maintenance of the culture in RPMI. **(B)** Barcode recovery of mPDAC3-RPMI cells either maintained in RPMI or transitioned to grow in TIFM. **(C)** Gini index for barcode distribution of mPDAC3-RPMI cells either maintained in RPMI or transitioned to grow in TIFM. **(D)** Correlation of log2 fold change in barcode abundance between mPDAC-RPMI cells transitioned into TIFM or maintained in RPMI. For D, Spearman's rank correlation test was used to determine significant correlation in barcode abundance change between culture conditions.

Figure 3 – Figure supplement 1: TIFM cultures have intact on-target activity and cellular responses to SN-38 treatment but do not undergo apoptosis. (A) Immunoblots for γH2AX and H2AX in the indicated

mPDAC cell line and culture condition following treatment with 10 μM SN-38 for 18 hours. **(B)** Alkaline comet assay of mPDAC1-RPMI and mPDAC1-TIFM cells treated with 10 μM SN-38 (RPMI n = 45, TIFM n = 70) or vehicle (RPMI n = 55, TIFM n = 70) for 18 hours. **(C)** Immunoblots for γH2AX, BIM, and Cleaved Caspase-3 in mPDAC1-RPMI and mPDAC1-TIFM cells treated with 10 μM SN-38 Gemcitabine over time at the indicated timepoints. For B, unpaired t-tests were performed to determine significance of differences between sample conditions. **** p≤0.0001.

Figure 3 – Figure supplement 2: Exogenous thymidine in TIFM suppresses on-target activity of 5-fluorouracil. (A) Immunoblots for γH2AX and H2AX in the indicated mPDAC cell line and culture condition following treatment with 5 μM 5-FU for 18 hours. **(B)** Alkaline comet assay of mPDAC1-RPMI and mPDAC1-TIFM cells treated with 5 μM 5-FU (RPMI n = 38, TIFM n = 34, RPMI + thymidine n = 46) or vehicle (RPMI n = 38, TIFM n = 50) for 18 hours. **(C)** Diagram of metabolic routes for thymidylate nucleotide synthesis. Cells possess a *de novo* synthesis route dependent on the activity of TYMS, the target of 5-fluorouracil. With loss of TYMS function, thymidylate nucleotide pools may still be maintained through a salvage pathway, dependent on the presence of exogenous thymidine in the environment and TK1 activity. **(D)** Cell viability of mPDAC1-RPMI cells measured by IncuCyte cell viability assay following treatment with indicated concentrations of 5-FU in the presence or absence of the indicated concentrations of thymidine after 72 hours (n = 3). For B, unpaired t-test was performed to determine significance of differences between sample conditions. For D, the area under the curve (AUC) was calculated and unpaired t-test was performed to determine significance of differences of AUC for the indicated cultures. *** p≤0.001, and **** p≤0.0001.

Figure 3 – Figure supplement 3: RMC-7977 retains on-target activity in TIFM-cultured PDAC cells. (A) Immunoblots for phospho-ERK and ERK in mPDAC1-RPMI and mPDAC1-TIFM cells treated with 2.5 μM RMC-7977 or vehicle for 24 hours.

Figure 3 – Figure supplement 4: Upregulation of pro-apoptotic BCL2 family members in mPDAC1-TIFM and mPDAC1-RPMI cells in response to gemcitabine. (A) Heatmap of normalized count values for known pro-apoptotic BH3-only genes following RNA-seq analysis of mPDAC1-RPMI and mPDAC1-TIFM cells treated with 125 nM gemcitabine or vehicle for 24 hours.

Figure 3 – Figure supplement 5: Cells under chronic nutrient stress acquire impaired apoptotic potential. (A) Diagram of experimental workflow for generating RPMI → TIFM cultures. Parental mPDAC1-RPMI adapted cultures are placed in TIFM containing 1% RPMI-1640 (V/V) for 2 weeks. Following this period, cells are transferred into 100% TIFM medium for 4 weeks prior to experimentation. **(B)** Immunoblots for γH2AX, BIM, and Cleaved Caspase-3 in mPDAC1-RPMI or mPDAC1-RPMI → TIFM cells treated with 150 nM gemcitabine over time at the indicated timepoints. **(C)** Relative mitochondrial depolarization of mPDAC1-RPMI and mPDAC1- RPMI → TIFM cells in response to treatment with recombinant BIM peptide at the indicated concentrations (n = 3). **(D)** Diagram of experimental workflow for generating chronically low arginine stressed PDAC cultures. Parental mPDAC1-RPMI adapted cultures are placed in RPMI containing 10 μM Arginine for 6 weeks prior to experimentation. **(E)** Immunoblots for γH2AX, BIM, and Cleaved Caspase-3 in mPDAC1-RPMI or mPDAC1 low arginine cultured cells treated with 150 nM gemcitabine over time at the indicated timepoints. **(F)** Relative mitochondrial depolarization of mPDAC1-RPMI and mPDAC1 low arginine cultured cells in response to treatment with recombinant BIM peptide at the indicated concentrations (n = 3). For C,F, the area under the curve (AUC) was calculated and unpaired t-tests were performed to determine significance of differences in AUC for the indicated sample conditions. * p≤0.05 and *** p≤0.001.

Figure 3 – Figure supplement 6: Mcl-1 overexpression in mPDAC TIFM cultures rescues synergistic cell death between BCL-XL targeting mimetic compounds and chemotherapy. (A) Cell viability of mPDAC1-TIFM cells measured by IncuCyte cell viability assay following transduction with *Mcl-1* overexpression or empty vector constructs and treatment with the indicated drug conditions (Gemcitabine, 150 nM), (A1331852, 1 μM), (Navitoclax, 1 μM) for 72hrs. Unpaired t-tests were performed to determine significance in cell viability measurements. *** p≤0.001, and **** p≤0.0001.

References

Abbott KL, Ali A, Casalena D, Do BT, Ferreira R, Cheah JH, Soule CK, Deik A, Kunchok T, Schmidt DR, Renner S, Honeder SE, Wu M, Chan SH, Tseyang T, Stoltzfus AT, Michel SLJ, Greaves D, Hsu PP, Ng CW, Zhang CJ, Farsidjani A, Kent JR, Madariaga MLL, Gramatikov IMT, Matheson NJ, Lewis CA, Clish CB, Rees MG, Roth JA, Griner LM, Muir A, Auld DS, Vander Heiden MG. 2023. Screening in serum-derived medium reveals differential response to compounds targeting metabolism. *Cell Chem Biol* **30**:1156-1168.e7.

Acanda de la Rocha AM, Berlow NE, Azzam DJ. 2025. Functional precision medicine: the future of cancer care. *Trends Mol Med* **31**:404–408.

Alcon C, Kovatcheva M, Morales-Sánchez P, López-Polo V, Torres T, Puig S, Lu A, Samitier J, Enrich C, Serrano M, Montero J. 2025. HRK downregulation and augmented BCL-xL binding to BAK confer apoptotic protection to therapy-induced senescent melanoma cells. *Cell Death Differ* **32**:646–656.

Amakye D, Jagani Z, Dorsch M. 2013. Unraveling the therapeutic potential of the Hedgehog pathway in cancer. *Nat Med* **19**:1410–1422.

American Cancer Society. Cancer Facts & Figures 2023. 2023. . Atlanta, Georgia.: American Cancer Society.

Apiz Saab JJ, Dzierozynski LN, Jonker PB, AminiTabrizi R, Shah H, Menjivar RE, Scott AJ, Nwosu ZC, Zhu Z, Chen RN, Oh M, Sheehan C, Wahl DR, Pasca di Magliano M, Lyssiotis CA, Macleod KF, Weber CR, Muir A. 2023. Pancreatic tumors exhibit myeloid-driven amino acid stress and upregulate arginine biosynthesis. *Elife* **12**. doi:10.7554/eLife.81289

Argani P, Iacobuzio-Donahue C, Ryu B, Rosty C, Goggins M, Wilentz R, Murugesan S, Leach S, Jaffee E, Yeo C, Cameron J, Kern S, Hruban R. 2001. Mesothelin is overexpressed in the vast majority of ductal adenocarcinomas of the pancreas: identification of a new pancreatic cancer marker by serial analysis of gene expression (SAGE). *Clin Cancer Res* **7**:3862–3868.

Badia-I-Mompel P, Vélez Santiago J, Braunger J, Geiss C, Dimitrov D, Müller-Dott S, Taus P, Dugourd A, Holland CH, Ramirez Flores RO, Saez-Rodriguez J. 2022. decoupleR: ensemble of computational methods to infer biological activities from omics data. *Bioinform Adv* **2**:vbac016.

Bankhead P, Loughrey MB, Fernández JA, Dombrowski Y, McArt DG, Dunne PD, McQuaid S, Gray RT, Murray LJ, Coleman HG, James JA, Salto-Tellez M, Hamilton PW. 2017. QuPath: Open source software for digital pathology image analysis. *Sci Rep* **7**:16878.

Basu A, Bodycombe NE, Cheah JH, Price EV, Liu K, Schaefer GI, Ebright RY, Stewart ML, Ito D, Wang S, Bracha AL, Liefeld T, Wawer M, Gilbert JC, Wilson AJ, Stransky N, Kryukov GV, Dancik V, Barretina J, Garraway LA, Hon CS-Y, Munoz B, Bittker JA, Stockwell BR, Khabele D, Stern AM, Clemons PA, Shamji AF, Schreiber SL. 2013. An interactive resource to identify cancer genetic and lineage dependencies targeted by small molecules. *Cell* **154**:1151–1161.

Beatty GL, Werba G, Lyssiotis CA, Simeone DM. 2021. The biological underpinnings of therapeutic resistance in pancreatic cancer. *Genes Dev*. doi:10.1101/gad.348523.121

Becker JH, Metropulos AE, Spaulding C, Marinelarena AM, Shields MA, Principe DR, Pham TD, Munshi HG. 2024. Targeting BCL2 with venetoclax enhances the efficacy of the KRASG12D inhibitor MRTX1133 in pancreatic cancer. *Cancer Res*. doi:10.1158/0008-5472.CAN-23-3574

Bernard V, Ku L-T, Wang T, Acevedo-Diaz A, Rajapakshe KI, Jacobson G, Tovar D, Min J, Pei G, Tat C, Suresh A, Tzeng C-WD, Katz MHG, Bhutani MS, Wang H, Wolff RA, Haymaker C, Ludmir EB, Huang H, Chen X, Li L, Koong AC, Wang L, Navin NE, Jiang D, Li Z, Maitra A, Koay EJ. 2025. A spatial atlas of chemoradiation therapy in pancreatic cancer identifies cellular and microenvironmental determinants of persister populations. *bioRxiv*. doi:10.1101/2025.06.20.660757

Beutel AK, Schütte L, Scheible J, Roger E, Müller M, Perkhofer L, Kestler AMTU, Kraus JM, Kestler HA, Barth TFE, Lemke J, Kornmann M, Ettrich TJ, Gout J, Seufferlein T, Kleger A. 2021. A prospective feasibility trial to challenge patient-derived pancreatic cancer organoids in predicting treatment response. *Cancers* **13**:2539.

Bhang H-EC, Ruddy DA, Krishnamurthy Radhakrishna V, Caushi JX, Zhao R, Hims MM, Singh AP, Kao I, Rakiec D, Shaw P, Balak M, Raza A, Ackley E, Keen N, Schlabach MR, Palmer M, Leary RJ, Chiang DY, Sellers WR, Michor F, Cooke VG, Korn JM, Stegmeier F. 2015. Studying clonal dynamics in response to cancer therapy using high-complexity barcoding. *Nat Med* **21**:440–448.

Blanco FF, Jimbo M, Wulfkuhle J, Gallagher I, Deng J, Enyenihi L, Meisner-Kober N, Londin E, Rigoutsos I, Sawicki JA, Risbud MV, Witkiewicz AK, McCue PA, Jiang W, Rui H, Yeo CJ, Petricoin E, Winter JM,

Brody JR. 2016. The mRNA-binding protein HuR promotes hypoxia-induced chemoresistance through posttranscriptional regulation of the proto-oncogene PIM1 in pancreatic cancer cells. *Oncogene* **35**:2529–2541.

Boilève A, Cartry J, Goudarzi N, Bedja S, Mathieu JRR, Bani M-A, Nicolle R, Mouawia A, Bouyakoub R, Nicotra C, Ngo-Camus M, Job B, Lipson K, Boige V, Valéry M, Tarabay A, Dartigues P, Tselikas L, de Baere T, Italiano A, Cosconea S, Gelli M, Fernandez-de-Sevilla E, Annereau M, Malka D, Smolenschi C, Ducreux M, Hollebecque A, Jaulin F. 2024. Organoids for functional precision medicine in advanced pancreatic cancer. *Gastroenterology*. doi:10.1053/j.gastro.2024.05.032

Boj SF, Hwang C-I, Baker LA, Chio IIC, Engle DD, Corbo V, Jager M, Ponz-Sarvise M, Tiriac H, Spector MS, Gracanin A, Oni T, Yu KH, van Boxtel R, Huch M, Rivera KD, Wilson JP, Feigin ME, Öhlund D, Handly-Santana A, Ardito-Abraham CM, Ludwig M, Elyada E, Alagesan B, Biffi G, Yordanov GN, Delcuze B, Creighton B, Wright K, Park Y, Morsink FHM, Molenaar IQ, Borel Rinkes IH, Cuppen E, Hao Y, Jin Y, Nijman IJ, Iacobuzio-Donahue C, Leach SD, Pappin DJ, Hammell M, Klimstra DS, Basturk O, Hruban RH, Offerhaus GJ, Vries RGJ, Clevers H, Tuveson DA. 2015. Organoid models of human and mouse ductal pancreatic cancer. *Cell* **160**:324–338.

Broderick C, Mezzadra R, Sisso EM, Mbuga F, Raghulan R, Chaves Perez A, Kulick A, Jiang L, Jiang J, Ho Y-J, Simon J, Rosiek E, Chan E, Filliol A, Chaligne R, de Stanchina E, Pechuan-Jorge X, Schietinger A, Singh M, Lowe SW. 2025. A RAS(ON) multi-selective inhibitor combination therapy triggers long-term tumor control through senescence-associated tumor-immune equilibrium in PDAC. *Cancer Discov* OF1–OF23.

Chauhan VP, Boucher Y, Ferrone CR, Roberge S, Martin JD, Stylianopoulos T, Bardeesy N, DePinho RA, Padera TP, Munn LL, Jain RK. 2014. Compression of pancreatic tumor blood vessels by hyaluronan is caused by solid stress and not interstitial fluid pressure. *Cancer Cell*.

Childs BG, Baker DJ, Kirkland JL, Campisi J, van Deursen JM. 2014. Senescence and apoptosis: dueling or complementary cell fates? *EMBO Rep* **15**:1139–1153.

Choi S, Chen Z, Tang LH, Fang Y, Shin SJ, Panarelli NC, Chen Y-T, Li Y, Jiang X, Du Y-CN. 2016. Bcl-xL promotes metastasis independent of its anti-apoptotic activity. *Nat Commun* **7**:10384.

Conroy T, Desseigne F, Ychou M, Bouché O, Guimbaud R, Bécouarn Y, Adenis A, Raoul J-L, Gourgou-Bourgade S, de la Fouchardière C, Bennouna J, Bachet J-B, Khemissa-Akouz F, Péré-Vergé D, Delbaldo C, Assenat E, Chauffert B, Michel P, Montoto-Grillot C, Ducreux M, Groupe Tumeurs Digestives of Unicancer, PRODIGE Intergroup. 2011. FOLFIRINOX versus gemcitabine for metastatic pancreatic cancer. *N Engl J Med* **364**:1817–1825.

Corsello SM, Nagari RT, Spangler RD, Rossen J, Kocak M, Bryan JG, Humeidi R, Peck D, Wu X, Tang AA, Wang VM, Bender SA, Lemire E, Narayan R, Montgomery P, Ben-David U, Garvie CW, Chen Y, Rees MG, Lyons NJ, McFarland JM, Wong BT, Wang L, Dumont N, O'Hearn PJ, Stefan E, Doench JG, Harrington CN, Greulich H, Meyerson M, Vazquez F, Subramanian A, Roth JA, Bittker JA, Boehm JS, Mader CC, Tsherniak A, Golub TR. 2020. Discovering the anti-cancer potential of non-oncology drugs by systematic viability profiling. *Nat Cancer* **1**:235–248.

Dalin S, Sullivan MR, Lau AN, Grauman-Boss B, Mueller HS, Kreidl E, Fenoglio S, Luengo A, Lees JA, Vander Heiden MG, Lauffenburger DA, Hemann MT. 2019. Deoxycytidine Release from Pancreatic Stellate Cells Promotes Gemcitabine Resistance. *Cancer Res* **79**:5723–5733.

Davis RJ. 2000. Signal transduction by the JNK group of MAP kinases. *Cell* **103**:239–252.

Dilly J, Hoffman MT, Abbassi L, Li Z, Paradiso F, Parent BD, Hennessey CJ, Jordan AC, Morgado M, Dasgupta S, Uribe GA, Yang A, Kapner KS, Hambitzer FP, Qiang L, Feng H, Geisberg J, Wang J, Evans KE, Lyu H, Schalck A, Feng N, Lopez AM, Bristow CA, Kim MP, Rajapakshe KI, Bahrambeigi V, Roth JA, Garg K, Guerrero PA, Stanger BZ, Cristea S, Lowe SW, Baslan T, Van Allen EM, Mancias JD, Chan E, Anderson A, Katlinskaya YV, Shalek AK, Hong DS, Pant S, Hallin J, Anderes K, Olson P, Heffernan TP, Chugh S, Christensen JG, Maitra A, Wolpin BM, Raghavan S, Nowak JA, Winter PS, Dougan SK, Aguirre AJ. 2024. Mechanisms of resistance to oncogenic KRAS inhibition in pancreatic cancer. *Cancer Discov* **14**:2135–2161.

Driehuis E, Gracanin A, Vries RGJ, Clevers H, Boj SF. 2020. Establishment of pancreatic organoids from normal tissue and tumors. *STAR Protoc* **1**:100192.

D'Urso A, Brickner JH. 2014. Mechanisms of epigenetic memory. *Trends Genet* **30**:230–236.

Edlich F, Banerjee S, Suzuki M, Cleland MM, Arnoult D, Wang C, Neutzner A, Tjandra N, Youle RJ. 2011. Bcl-x(L) retrotranslocates Bax from the mitochondria into the cytosol. *Cell* **145**:104–116.

Erstad DJ, Sojoodi M, Taylor MS, Ghoshal S, Razavi AA, Graham-O'Regan KA, Bardeesy N, Ferrone CR, Lanuti M, Caravan P, Tanabe KK, Fuchs BC. 2018. Orthotopic and heterotopic murine models of pancreatic cancer and their different responses to FOLFIRINOX chemotherapy. *Dis Model Mech* **11**. doi:10.1242/dmm.034793

Feig C, Gopinathan A, Neesse A, Chan DS, Cook N, Tuveson DA. 2012. The pancreas cancer microenvironment. *Clin Cancer Res* **18**:4266–4276.

Flickinger KM, Wilson KM, Rossiter NJ, Hunger AL, Vishwasrao PV, Lee TD, Mellado Fritz CA, Richards RM, Hall MD, Cantor JR. 2024. Conditional lethality profiling reveals anticancer mechanisms of action and drug-nutrient interactions. *Sci Adv* **10**:eadq3591.

García-Jiménez C, Goding CR. 2019. Starvation and Pseudo-Starvation as Drivers of Cancer Metastasis through Translation Reprogramming. *Cell Metab* **29**:254–267.

Gonçalves AC, Richiardone E, Jorge J, Polónia B, Xavier CPR, Salaroglio IC, Riganti C, Vasconcelos MH, Corbet C, Sarmento-Ribeiro AB. 2021. Impact of cancer metabolism on therapy resistance - Clinical implications. *Drug Resist Updat* **59**:100797.

Graeber TG, Osmanian C, Jacks T, Housman DE, Koch CJ, Lowe SW, Giaccia AJ. 1996. Hypoxia-mediated selection of cells with diminished apoptotic potential in solid tumours. *Nature* **379**:88–91.

Guo JA, Gong D, Evans K, Takahashi K, Jambhale AD, Shiau C, Yu P, Wang S, Wu WW, Chugh S, Kapner KS, Dilly J, Zhao D, Chen P, Smith EL, Mancias JD, Vazquez F, Singh H, Hwang WL, Aguirre AJ. 2025. Integrative genomic identification of therapeutic targets for pancreatic cancer. *Cell Rep* **44**. doi:10.1016/j.celrep.2025.116191

Gyori BM, Venkatachalam G, Thiagarajan PS, Hsu D, Clement M-V. 2014. OpenComet: an automated tool for comet assay image analysis. *Redox Biol* **2**:457–465.

Hafner M, Niepel M, Chung M, Sorger PK. 2016. Growth rate inhibition metrics correct for confounders in measuring sensitivity to cancer drugs. *Nat Methods* **13**:521–527.

Hakim N, Patel R, Devoe C, Saif MW. 2019. Why HALO 301 Failed and Implications for Treatment of Pancreatic Cancer. *Pancreas* **3**:e1–e4.

Halbrook CJ, Pontious C, Kovalenko I, Lapienyte L, Dreyer S, Lee H-J, Thurston G, Zhang Y, Lazarus J, Sajjakulnukit P, Hong HS, Kremer DM, Nelson BS, Kemp S, Zhang L, Chang D, Biankin A, Shi J, Frankel TL, Crawford HC, Morton JP, Pasca di Magliano M, Lyssiotis CA. 2019. Macrophage-Released Pyrimidines Inhibit Gemcitabine Therapy in Pancreatic Cancer. *Cell Metab* **29**:1390-1399.e6.

Hallin J, Bowcut V, Calinisan A, Briere DM, Hargis L, Engstrom LD, Laguer J, Medwid J, Vanderpool D, Lifset E, Trinh D, Hoffman N, Wang X, David Lawson J, Gunn RJ, Smith CR, Thomas NC, Martinson M, Bergstrom A, Sullivan F, Bouhana K, Winski S, He L, Fernandez-Banet J, Pavlicek A, Haling JR, Rahbaek L, Marx MA, Olson P, Christensen JG. 2022. Anti-tumor efficacy of a potent and selective non-covalent KRASG12D inhibitor. *Nat Med* **28**:2171–2182.

Han S, Tushoski-Alemán GW, Zhang P, Zheng G, Zhou D, Huo Z, Licht J, George TJ, Allegra C, Trevino JG, Hughes SJ. 2025. A novel regimen for pancreatic ductal adenocarcinoma targeting MEK, BCL-xL, and EGFR. *Neoplasia* **59**:101070.

Hänggi K, Ruffell B. 2023. Cell death, therapeutics, and the immune response in cancer. *Trends Cancer* **9**:381–396.

Hasselluhn MC, Decker-Farrell AR, Vlahos L, Thomas DH, Curiel-Garcia A, Maurer HC, Wasko UN, Tomassoni L, Sastra SA, Palermo CF, Dalton TC, Ma A, Li F, Tolosa EJ, Hibshoosh H, Fernandez-Zapico ME, Muir A, Califano A, Olive KP. 2023. Tumor Explants Elucidate a Cascade of Paracrine SHH, WNT, and VEGF Signals Driving Pancreatic Cancer Angiosuppression. *Cancer Discov*. doi:10.1158/2159-8290.CD-23-0240

Hessmann E, Patzak MS, Klein L, Chen N, Kari V, Ramu I, Bapiro TE, Frese KK, Gopinathan A, Richards FM, Jodrell DI, Verbeke C, Li X, Heuchel R, Löhr JM, Johnsen SA, Gress TM, Ellenrieder V, Neesse A. 2018. Fibroblast drug scavenging increases intratumoural gemcitabine accumulation in murine pancreas cancer. *Gut* **67**:497–507.

Hosein AN, Brekken RA, Maitra A. 2020. Pancreatic cancer stroma: an update on therapeutic targeting strategies. *Nat Rev Gastroenterol Hepatol*. doi:10.1038/s41575-020-0300-1

Ikezawa K, Hikita H, Shigekawa M, Iwahashi K, Eguchi H, Sakamori R, Tatsumi T, Takehara T. 2017. Increased Bcl-xL Expression in Pancreatic Neoplasia Promotes Carcinogenesis by Inhibiting Senescence and Apoptosis. *Cell Mol Gastroenterol Hepatol* **4**:185-200.e1.

Iorio F, Knijnenburg TA, Vis DJ, Bignell GR, Menden MP, Schubert M, Aben N, Gonçalves E, Barthorpe S, Lightfoot H, Cokelaer T, Greninger P, van Dyk E, Chang H, de Silva H, Heyn H, Deng X, Egan RK, Liu

Q, Mironenko T, Mitropoulos X, Richardson L, Wang J, Zhang T, Moran S, Sayols S, Soleimani M, Tamborero D, Lopez-Bigas N, Ross-Macdonald P, Esteller M, Gray NS, Haber DA, Stratton MR, Benes CH, Wessels LFA, Saez-Rodriguez J, McDermott U, Garnett MJ. 2016. A landscape of pharmacogenomic interactions in cancer. *Cell* **166**:740–754.

Jacobetz MA, Chan DS, Neesse A, Bapiro TE, Cook N, Frese KK, Feig C, Nakagawa T, Caldwell ME, Zecchini HI, Lolkema MP, Jiang P, Kultti A, Thompson CB, Maneval DC, Jodrell DI, Frost GI, Shepard HM, Skepper JN, Tuveson DA. 2013. Hyaluronan impairs vascular function and drug delivery in a mouse model of pancreatic cancer. *Gut* **62**:112–120.

Johnson GL, Nakamura K. 2007. The c-jun kinase/stress-activated pathway: regulation, function and role in human disease. *Biochim Biophys Acta* **1773**:1341–1348.

Jonker PB, Sadullozoda M, Cognet G, Saab JJA, Sokol KH, Wu VX, Kumari D, Sheehan C, Ozgurses ME, Agovino D, Croley G, Patel SA, Bock-Hughes A, Macleod KF, Shah H, Coloff JL, Lien EC, Muir A. 2025. Microenvironmental arginine restriction sensitizes pancreatic cancers to polyunsaturated fatty acids by suppression of lipid synthesis. *eLife*. doi:10.7554/elife.106492.1

Kahn BM, Lucas A, Alur RG, Wengyn MD, Schwartz GW, Li J, Sun K, Maurer HC, Olive KP, Faryabi RB, Stanger BZ. 2021. The vascular landscape of human cancer. *J Clin Invest* **131**. doi:10.1172/JCI136655

Kale J, Osterlund EJ, Andrews DW. 2018. BCL-2 family proteins: changing partners in the dance towards death. *Cell Death Differ* **25**:65–80.

Kemp SB, Cheng N, Markosyan N, Sor R, Kim I-K, Hallin J, Shoush J, Quinones L, Brown NV, Bassett JB, Joshi N, Yuan S, Smith M, Vostrejs WP, Perez-Vale KZ, Kahn B, Mo F, Donahue TR, Radu CG, Clendenin C, Christensen JG, Vonderheide RH, Stanger BZ. 2023. Efficacy of a small-molecule inhibitor of KrasG12D in immunocompetent models of pancreatic cancer. *Cancer Discov* **13**:298–311.

Kim CY, Tsai M-H, Osmanian C, Graeber T, Lee JE, Giffard R, DiPaolo J, Peehl D, Giaccia A. 1997. Selection of human cervical epithelial cells that possess reduced apoptotic potential to low-oxygen conditions. *Cancer Res* **57**:4200–4204.

Knight JC, Mosley MJ, Bravo LC, Kersemans V, Allen PD, Mukherjee S, O'Neill E, Cornelissen B. 2017. 89Zr-anti-γH2AX-TAT but not 18F-FDG Allows Early Monitoring of Response to Chemotherapy in a Mouse Model of Pancreatic Ductal Adenocarcinoma. *Clin Cancer Res* **23**:6498–6504.

Komar G, Kauhanen S, Liukko K, Seppänen M, Kajander S, Ovaska J, Nuutila P, Minn H. 2009. Decreased blood flow with increased metabolic activity: a novel sign of pancreatic tumor aggressiveness. *Clin Cancer Res* **15**:5511–5517.

Kramer RM, Russell J, Humm JL. 2015. Distribution of Gemcitabine Is Nearly Homogenous in Two Orthotopic Murine Models of Pancreatic Cancer. *Cancer Biother Radiopharm* **30**:299–304.

Lee M-S, Dennis C, Naqvi I, Dailey L, Lorzadeh A, Ye G, Zaytouni T, Adler A, Hitchcock DS, Lin L, Hoffman MT, Bhuiyan AM, Barth JL, Machacek ME, Mino-Kenudson M, Dougan SK, Jadhav U, Clish CB, Kalaany NY. 2023. Ornithine aminotransferase supports polyamine synthesis in pancreatic cancer. *Nature* 1–9.

Letai A. 2017. Functional precision cancer medicine-moving beyond pure genomics. *Nat Med* **23**:1028–1035.

Letai A, Bhola P, Welm AL. 2022. Functional precision oncology: Testing tumors with drugs to identify vulnerabilities and novel combinations. *Cancer Cell* **40**:26–35.

Letai A, de The H. 2024. Conventional chemotherapy: millions of cures, unresolved therapeutic index. *Nat Rev Cancer* 1–10.

Levy MJ, Alberts SR, Bamlet WR, Burch PA, Farnell MB, Gleeson FC, Haddock MG, Kendrick ML, Oberg AL, Petersen GM, Takahashi N, Chari ST. 2017. EUS-guided fine-needle injection of gemcitabine for locally advanced and metastatic pancreatic cancer. *Gastrointest Endosc* **86**:161–169.

Li C, Liu Y, Liu C, Chen F, Xie Y, Zeh HJ, Yu C, Liu J, Tang D, Kang R. 2025. AGER-dependent macropinocytosis drives resistance to KRAS-G12D-targeted therapy in advanced pancreatic cancer. *Sci Transl Med* **17**:eadp4986.

Li J, Qian W, Qin T, Xiao Y, Cheng L, Cao J, Chen X, Ma Q, Wu Z. 2019. Mouse-Derived Allografts: A Complementary Model to the KPC Mice on Researching Pancreatic Cancer In Vivo. *Comput Struct Biotechnol J* **17**:498–506.

Loo LSW, Soetedjo AAP, Lau HH, Ng NHJ, Ghosh S, Nguyen L, Krishnan VG, Choi H, Roca X, Hoon S, Teo AKK. 2020. BCL-xL/BCL2L1 is a critical anti-apoptotic protein that promotes the survival of differentiating pancreatic cells from human pluripotent stem cells. *Cell Death Dis* **11**:378.

Loukas I, Simeoni F, Milan M, Inglese P, Patel H, Goldstone R, East P, Strohbuecker S, Mitter R, Talsania B, Tang W, Ratcliffe CDH, Sahai E, Shahrezaei V, Scaffidi P. 2022. Selective advantage of epigenetically disrupted cancer cells via phenotypic inertia. *Cancer Cell*. doi:10.1016/j.ccell.2022.10.002

Mahadevan KK, McAndrews KM, LeBleu VS, Yang S, Lyu H, Li B, Sockwell AM, Kirtley ML, Morse SJ, Moreno Diaz BA, Kim MP, Feng N, Lopez AM, Guerrero PA, Paradiso F, Sugimoto H, Arian KA, Ying H, Barekatain Y, Sthanam LK, Kelly PJ, Maitra A, Heffernan TP, Kalluri R. 2023. KRASG12D inhibition reprograms the microenvironment of early and advanced pancreatic cancer to promote FAS-mediated killing by CD8+ T cells. *Cancer Cell*. doi:10.1016/j.ccell.2023.07.002

Mancini C, Lori G, Pranzini E, Taddei ML. 2023. Metabolic challengers selecting tumor-persistent cells. *Trends Endocrinol Metab*. doi:10.1016/j.tem.2023.11.005

Martin DS, Stolfi RL, Sawyer RC, Nayak R, Spiegelman S, Young CW, Woodcock T. 1980. An overview of thymidine. *Cancer* **45**:1117–1128.

Masoud R, Reyes-Castellanos G, Lac S, Garcia J, Dou S, Shintu L, Abdel Hadi N, Gicquel T, El Kaoutari A, Diémé B, Tranchida F, Cormareche L, Borge L, Gayet O, Pasquier E, Dusetti N, Iovanna J, Carrier A. 2020. Targeting Mitochondrial Complex I Overcomes Chemoresistance in High OXPHOS Pancreatic Cancer. *Cell Rep Med* **1**:100143.

Matthews JM, Schuster B, Kashaf SS, Liu P, Ben-Yishay R, Ishay-Ronen D, Izumchenko E, Shen L, Weber CR, Bielski M, Kupfer SS, Bilgic M, Rzhetsky A, Tay S. 2022. OrganoID: A versatile deep learning platform for tracking and analysis of single-organoid dynamics. *PLoS Comput Biol* **18**:e1010584.

Menjivar RE, Nwosu ZC, Du W, Donahue KL, Hong HS, Espinoza C, Brown K, Velez-Delgado A, Yan W, Lima F, Bischoff A, Kadiyala P, Salas-Escabillas D, Crawford HC, Bednar F, Carpenter E, Zhang Y, Halbrook CJ, Lyssiotis CA, Pasca di Magliano M. 2023. Arginase 1 is a key driver of immune suppression in pancreatic cancer. *Elife* **12**:e80721.

Montano R, Khan N, Hou H, Seigne J, Ernstoff MS, Lewis LD, Eastman A. 2017. Cell cycle perturbation induced by gemcitabine in human tumor cells in cell culture, xenografts and bladder cancer patients: implications for clinical trial designs combining gemcitabine with a Chk1 inhibitor. *Oncotarget* **8**:67754–67768.

Muir A, Vander Heiden MG. 2018. The nutrient environment affects therapy. *Science* **360**:962–963.

Mullen NJ, Singh PK. 2023. Nucleotide metabolism: a pan-cancer metabolic dependency. *Nat Rev Cancer* **23**:275–294.

Oberstein PE, Olive KP. 2013. Pancreatic cancer: why is it so hard to treat? *Therap Adv Gastroenterol* **6**:321–337.

O'Hara M, Stashwick C, Haas AR, Tanyi JL. 2016. Mesothelin as a target for chimeric antigen receptor-modified T cells as anticancer therapy. *Immunotherapy* **8**:449–460.

Olive KP, Jacobetz MA, Davidson CJ, Gopinathan A, McIntyre D, Honess D, Madhu B, Goldgraben MA, Caldwell ME, Allard D, Frese KK, Denicola G, Feig C, Combs C, Winter SP, Ireland-Zecchini H, Reichelt S, Howat WJ, Chang A, Dhara M, Wang L, Rückert F, Grützmann R, Pilarsky C, Izeradjene K, Hingorani SR, Huang P, Davies SE, Plunkett W, Egorin M, Hruban RH, Whitebread N, McGovern K, Adams J, Iacobuzio-Donahue C, Griffiths J, Tuveson DA. 2009. Inhibition of Hedgehog signaling enhances delivery of chemotherapy in a mouse model of pancreatic cancer. *Science* **324**:1457–1461.

Orlen MI, Vostrejs WP, Sor R, McDevitt JC, Kemp SB, Kim I-K, Kramer AB, Tovbis Shifrin N, Markosyan N, Clendenin C, Singh M, Quintana E, Menard M, Vonderheide RH, Stanger BZ. 2025. T-cell dependency of tumor regressions and complete responses with RAS(ON) multi-selective inhibition in preclinical models of PDAC. *Cancer Discov*. doi:10.1158/2159-8290.CD-24-1475

Özdemir BC, Pentcheva-Hoang T, Carstens JL, Zheng X, Wu C-C, Simpson TR, Laklai H, Sugimoto H, Kahlert C, Novitskiy SV, De Jesus-Acosta A, Sharma P, Heidari P, Mahmood U, Chin L, Moses HL, Weaver VM, Maitra A, Allison JP, LeBleu VS, Kalluri R. 2014. Depletion of carcinoma-associated fibroblasts and fibrosis induces immunosuppression and accelerates pancreas cancer with reduced survival. *Cancer Cell* **25**:719–734.

Piper AA, Nott SE, Mackinnon WB, Tattersall MH. 1983. Critical modulation by thymidine and hypoxanthine of sequential methotrexate-5-fluorouracil synergism in murine L1210 cells. *Cancer Res* **43**:5101–5105.

Potter DS, Letai A. 2016. To Prime, or Not to Prime: That Is the Question. *Cold Spring Harb Symp Quant Biol* **81**:131–140.

Preston GA, Lyon TT, Yin Y, Lang JE, Solomon G, Annab L, Srinivasan DG, Alcorta DA, Barrett JC. 1996. Induction of apoptosis by c-Fos protein. *Mol Cell Biol* **16**:211–218.

Provenzano PP, Cuevas C, Chang AE, Goel VK, Von Hoff DD, Hingorani SR. 2012. Enzymatic targeting of the stroma ablates physical barriers to treatment of pancreatic ductal adenocarcinoma. *Cancer Cell* **21**:418–429.

Ramanathan RK, McDonough SL, Philip PA, Hingorani SR, Lacy J, Kortmansky JS, Thumar J, Chiorean EG, Shields AF, Behl D, Mehan PT, Gaur R, Seery T, Guthrie KA, Hochster HS. 2019. Phase IB/II

Randomized Study of FOLFIRINOX Plus Pegylated Recombinant Human Hyaluronidase Versus FOLFIRINOX Alone in Patients With Metastatic Pancreatic Adenocarcinoma: SWOG S1313. *J Clin Oncol* **37**:1062–1069.

Ravindran Menon D, Das S, Krepler C, Vultur A, Rinner B, Schauer S, Kashofer K, Wagner K, Zhang G, Bonyadi Rad E, Haass NK, Soyer HP, Gabrielli B, Somasundaram R, Hoefler G, Herlyn M, Schaider H. 2015. A stress-induced early innate response causes multidrug tolerance in melanoma. *Oncogene* **34**:4448–4459.

Rawat V, DeLear P, Prashanth P, Ozgurses ME, Tebeje A, Burns PA, Conger KO, Solís C, Hasnain Y, Novikova A, Endress JE, González-Sánchez P, Dong W, Stephanopoulos G, DeNicola GM, Harris IS, Sept D, Mason FM, Coloff JL. 2024. Drug screening in human physiologic medium identifies uric acid as an inhibitor of rigosertib efficacy. *JCI Insight* **9**:e174329.

Replogle JM, Saunders RA, Pogson AN, Hussmann JA, Lenail A, Guna A, Mascibroda L, Wagner EJ, Adelman K, Lithwick-Yanai G, Iremadze N, Oberstrass F, Lipson D, Bonnar JL, Jost M, Norman TM, Weissman JS. 2022. Mapping information-rich genotype-phenotype landscapes with genome-scale Perturb-seq. *Cell* **185**:2559-2575.e28.

Rhim AD, Oberstein PE, Thomas DH, Mirek ET, Palermo CF, Sastra SA, Dekleva EN, Saunders T, Becerra CP, Tattersall IW, Westphalen CB, Kitajewski J, Fernandez-Barrena MG, Fernandez-Zapico ME, Iacobuzio-Donahue C, Olive KP, Stanger BZ. 2014. Stromal elements act to restrain, rather than support, pancreatic ductal adenocarcinoma. *Cancer Cell* **25**:735–747.

Romero R, Sánchez-Rivera FJ, Westcott PMK, Mercer KL, Bhutkar A, Muir A, González Robles TJ, Lamboy Rodríguez S, Liao LZ, Ng SR, Li L, Colón CI, Naranjo S, Beytagh MC, Lewis CA, Hsu PP, Bronson RT, Vander Heiden MG, Jacks T. 2020. Keap1 mutation renders lung adenocarcinomas dependent on Slc33a1. *Nature Cancer*. doi:10.1038/s43018-020-0071-1

Ryan J, Letai A. 2013. BH3 profiling in whole cells by fluorimeter or FACS. *Methods* **61**:156–164.

Sanjana NE, Shalem O, Zhang F. 2014. Improved vectors and genome-wide libraries for CRISPR screening. *Nat Methods* **11**:783–784.

Sarosiek KA, Ni Chonghaile T, Letai A. 2013. Mitochondria: gatekeepers of response to chemotherapy. *Trends Cell Biol* **23**:612–619.

Scannell JW, Bosley J, Hickman JA, Dawson GR, Truebel H, Ferreira GS, Richards D, Treherne JM. 2022. Predictive validity in drug discovery: what it is, why it matters and how to improve it. *Nat Rev Drug Discov* **21**:915–931.

Sela Y, Li J, Maheswaran S, Norgard RJ, Yuan S, Hubbi ME, Doepner M, Xu JP, Ho ES, Mesaros C, Sheehan C, Croley G, Muir A, Blair IA, Shalem O, Dang CV, Stanger BZ. 2022. Bcl-xL enforces a slow-cycling state necessary for survival in the nutrient-deprived microenvironment of pancreatic cancer. *Cancer Res*. doi:10.1158/0008-5472.CAN-22-0431

Shah MA, Schwartz GK. 2001. Cell cycle-mediated drug resistance: An emerging concept in cancer Therapy1. https://aacrjournals.org/clincancerres/article-pdf/7/8/2168/2080283/df0801002168.pdf

Sheehan C, Muir A. 2025. What's on the menu?: metabolic constraints in the pancreatic tumor microenvironment. *J Clin Invest* **135**. doi:10.1172/jci191940

Sherman MH, Beatty GL. 2022. Tumor Microenvironment in Pancreatic Cancer Pathogenesis and Therapeutic Resistance. *Annu Rev Pathol*. doi:10.1146/annurev-pathmechdis-031621-024600

Shoemaker RH. 2006. The NCI60 human tumour cell line anticancer drug screen. *Nat Rev Cancer* **6**:813–823.

Strasser A, Vaux DL. 2020. Cell death in the origin and treatment of cancer. *Mol Cell* **78**:1045–1054.

Strickler JH, Satake H, George TJ, Yaeger R, Hollebecque A, Garrido-Laguna I, Schuler M, Burns TF, Coveler AL, Falchook GS, Vincent M, Sunakawa Y, Dahan L, Bajor D, Rha S-Y, Lemech C, Juric D, Rehn M, Ngarmchamnanrith G, Jafarinasabian P, Tran Q, Hong DS. 2023. Sotorasib in KRAS p.G12C-mutated advanced pancreatic cancer. *N Engl J Med* **388**:33–43.

Strittmatter N, Richards FM, Race AM, Ling S, Sutton D, Nilsson A, Wallez Y, Barnes J, Maglennon G, Gopinathan A, Brais R, Wong E, Serra MP, Atkinson J, Smith A, Wilson J, Hamm G, Johnson TI, Dunlop CR, Kaistha BP, Bunch J, Sansom OJ, Takats Z, Andrén PE, Lau A, Barry ST, Goodwin RJA, Jodrell DI. 2022. Method To Visualize the Intratumor Distribution and Impact of Gemcitabine in Pancreatic Ductal Adenocarcinoma by Multimodal Imaging. *Anal Chem* **94**:1795–1803.

Stylianopoulos T, Martin JD, Chauhan VP, Jain SR, Diop-Frimpong B, Bardeesy N, Smith BL, Ferrone CR, Hornicek FJ, Boucher Y, Munn LL, Jain RK. 2012. Causes, consequences, and remedies for growth-induced solid stress in murine and human tumors. *Proc Natl Acad Sci U S A* **109**:15101–15108.

Tait SWG, Parsons MJ, Llambi F, Bouchier-Hayes L, Connell S, Muñoz-Pinedo C, Green DR. 2010. Resistance to caspase-independent cell death requires persistence of intact mitochondria. *Dev Cell* **18**:802–813.

Tempero MA, Van Cutsem E, Sigal D, Oh D-Y, Fazio N, Macarulla T, Hitre E, Hammel P, Hendifar AE, Bates SE, Li C-P, De La Fouchardiere C, Heinemann V, Maraveyas A, Bahary N, Layos L, Sahai V, Zheng L, Lacy J, Bullock AJ. 2020. HALO 109-301: A randomized, double-blind, placebo-controlled, phase 3 study of pegvorhyaluronidase alfa (PEGPH20) + nab-paclitaxel/gemcitabine (AG) in patients (pts) with previously untreated hyaluronan (HA)-high metastatic pancreatic ductal adenocarcinoma (mPDA). *J Clin Orthod* **38**:638–638.

Thummuri D, Khan S, Underwood PW, Zhang P, Wiegand J, Zhang X, Budamagunta V, Sobh A, Tagmount A, Loguinov A, Riner AN, Akki AS, Williamson E, Hromas R, Vulpe CD, Zheng G, Trevino JG, Zhou D. 2022. Overcoming Gemcitabine Resistance in Pancreatic Cancer Using the BCL-XL-Specific Degrader DT2216. *Mol Cancer Ther* **21**:184–192.

Tiriac H, Belleau P, Engle DD, Plenker D, Deschênes A, Somerville TDD, Froeling FEM, Burkhart RA, Denroche RE, Jang G-H, Miyabayashi K, Young CM, Patel H, Ma M, LaComb JF, Palmaira RLD, Javed AA, Huynh JC, Johnson M, Arora K, Robine N, Shah M, Sanghvi R, Goetz AB, Lowder CY, Martello L, Driehuis E, LeComte N, Askan G, Iacobuzio-Donahue CA, Clevers H, Wood LD, Hruban RH, Thompson E, Aguirre AJ, Wolpin BM, Sasson A, Kim J, Wu M, Bucobo JC, Allen P, Sejpal DV, Nealon W, Sullivan JD, Winter JM, Gimotty PA, Grem JL, DiMaio DJ, Buscaglia JM, Grandgenett PM, Brody JR, Hollingsworth MA, O'Kane GM, Notta F, Kim E, Crawford JM, Devoe C, Ocean A, Wolfgang CL, Yu KH, Li E, Vakoc CR, Hubert B, Fischer SE, Wilson JM, Moffitt R, Knox J, Krasnitz A, Gallinger S, Tuveson DA. 2018. Organoid profiling identifies common responders to chemotherapy in pancreatic cancer. *Cancer Discov* **8**:1112–1129.

Todt F, Cakir Z, Reichenbach F, Emschermann F, Lauterwasser J, Kaiser A, Ichim G, Tait SWG, Frank S, Langer HF, Edlich F. 2015. Differential retrotranslocation of mitochondrial Bax and Bak. *EMBO J* **34**:67–80.

van Renterghem AWJ, van de Haar J, Voest EE. 2023. Functional precision oncology using patient-derived assays: bridging genotype and phenotype. *Nat Rev Clin Oncol* **20**:305–317.

Vincent T. DeVita, Jr., Theodore S. Lawrence, Steven A. Rosenberg. 2015. DeVita, Hellman, and Rosenberg's Cancer: Principles & Practice of Oncology. Baltimore, MD: Wolters Kluwer Health.

Von Hoff DD, Ervin T, Arena FP, Chiorean EG, Infante J, Moore M, Seay T, Tjulandin SA, Ma WW, Saleh MN, Harris M, Reni M, Dowden S, Laheru D, Bahary N, Ramanathan RK, Tabernero J, Hidalgo M, Goldstein D, Van Cutsem E, Wei X, Iglesias J, Renschler MF. 2013. Increased survival in pancreatic cancer with nab-paclitaxel plus gemcitabine. *N Engl J Med* **369**:1691–1703.

Wang P, Chen L-L, Xiong Y, Ye D. 2024. Metabolite regulation of epigenetics in cancer. *Cell Rep* **43**:114815.

Wasko UN, Jiang J, Dalton TC, Curiel-Garcia A, Edwards AC, Wang Y, Lee B, Orlen M, Tian S, Stalnecker CA, Drizyte-Miller K, Menard M, Dilly J, Sastra SA, Palermo CF, Hasselluhn MC, Decker-Farrell AR, Chang S, Jiang L, Wei X, Yang YC, Helland C, Courtney H, Gindin Y, Muonio K, Zhao R, Kemp SB, Clendenin C, Sor R, Vostrejs WP, Hibshman PS, Amparo AM, Hennessey C, Rees MG, Ronan MM, Roth JA, Brodbeck J, Tomassoni L, Bakir B, Socci ND, Herring LE, Barker NK, Wang J, Cleary JM, Wolpin BM, Chabot JA, Kluger MD, Manji GA, Tsai KY, Sekulic M, Lagana SM, Califano A, Quintana E, Wang Z, Smith JAM, Holderfield M, Wildes D, Lowe SW, Badgley MA, Aguirre AJ, Vonderheide RH, Stanger BZ, Baslan T, Der CJ, Singh M, Olive KP. 2024. Tumour-selective activity of RAS-GTP inhibition in pancreatic cancer. *Nature* **629**:927–936.

Wensink GE, Elias SG, Mullenders J, Koopman M, Boj SF, Kranenburg OW, Roodhart JML. 2021. Patient-derived organoids as a predictive biomarker for treatment response in cancer patients. *NPJ Precis Oncol* **5**:30.

Wilson PM, Danenberg PV, Johnston PG, Lenz H-J, Ladner RD. 2014. Standing the test of time: targeting thymidylate biosynthesis in cancer therapy. *Nat Rev Clin Oncol* **11**:282–298.

Wu T, Hu E, Xu S, Chen M, Guo P, Dai Z, Feng T, Zhou L, Tang W, Zhan L, Fu X, Liu S, Bo X, Yu G. 2021. clusterProfiler 4.0: A universal enrichment tool for interpreting omics data. *Innovation (Camb)* **2**:100141.

Yan Y, Han X, Qing Y, Condie AG, Gorityala S, Yang S, Xu Y, Zhang Y, Gerson SL. 2016. Inhibition of uracil DNA glycosylase sensitizes cancer cells to 5-fluorodeoxyuridine through replication fork collapse-induced DNA damage. *Oncotarget* **7**:59299–59313.

Zeng S, Pöttler M, Lan B, Grützmann R, Pilarsky C, Yang H. 2019. Chemoresistance in Pancreatic Cancer. *Int J Mol Sci* **20**. doi:10.3390/ijms20184504

Zhang H, Santana-Codina N, Yu Q, Poupault C, Campos C, Qin X, Sindoni N, Ciscar M, Padhye A, Kuljanin M, Wang J, Dorman MJ, Bross P, Aguirre AJ, Dougan SK, Sarosiek KA, Mancias JD. 2025. De novo

pyrimidine biosynthesis inhibition synergizes with BCL-XL targeting in pancreatic cancer. *Nat Commun* **16**:6987.

Zhang T, Li S, Tan YA, Chen X, Zhang C, Chen Z, Mishra B, Na JH, Choi S, Shin SJ, Damle P, Chougoni KK, Grossman SR, Wang D, Jiang X, Li Y, Hissong E, Chen Y-T, Xiang JZ, Du Y-CN. 2024. Bcl-xL is translocated to the nucleus via CtBP2 to epigenetically promote metastasis. *Cancer Lett* **604**:217240.

Zhou X, An J, Kurilov R, Brors B, Hu K, Peccerella T, Roessler S, Pfütze K, Schulz A, Wolf S, Hohmann N, Theile D, Sauter M, Burhenne J, Ei S, Heger U, Strobel O, Barry ST, Springfeld C, Tjaden C, Bergmann F, Büchler M, Hackert T, Fortunato F, Neoptolemos JP, Bailey P. 2023. Persister cell phenotypes contribute to poor patient outcomes after neoadjuvant chemotherapy in PDAC. *Nat Cancer* 1–20.

Figure 1

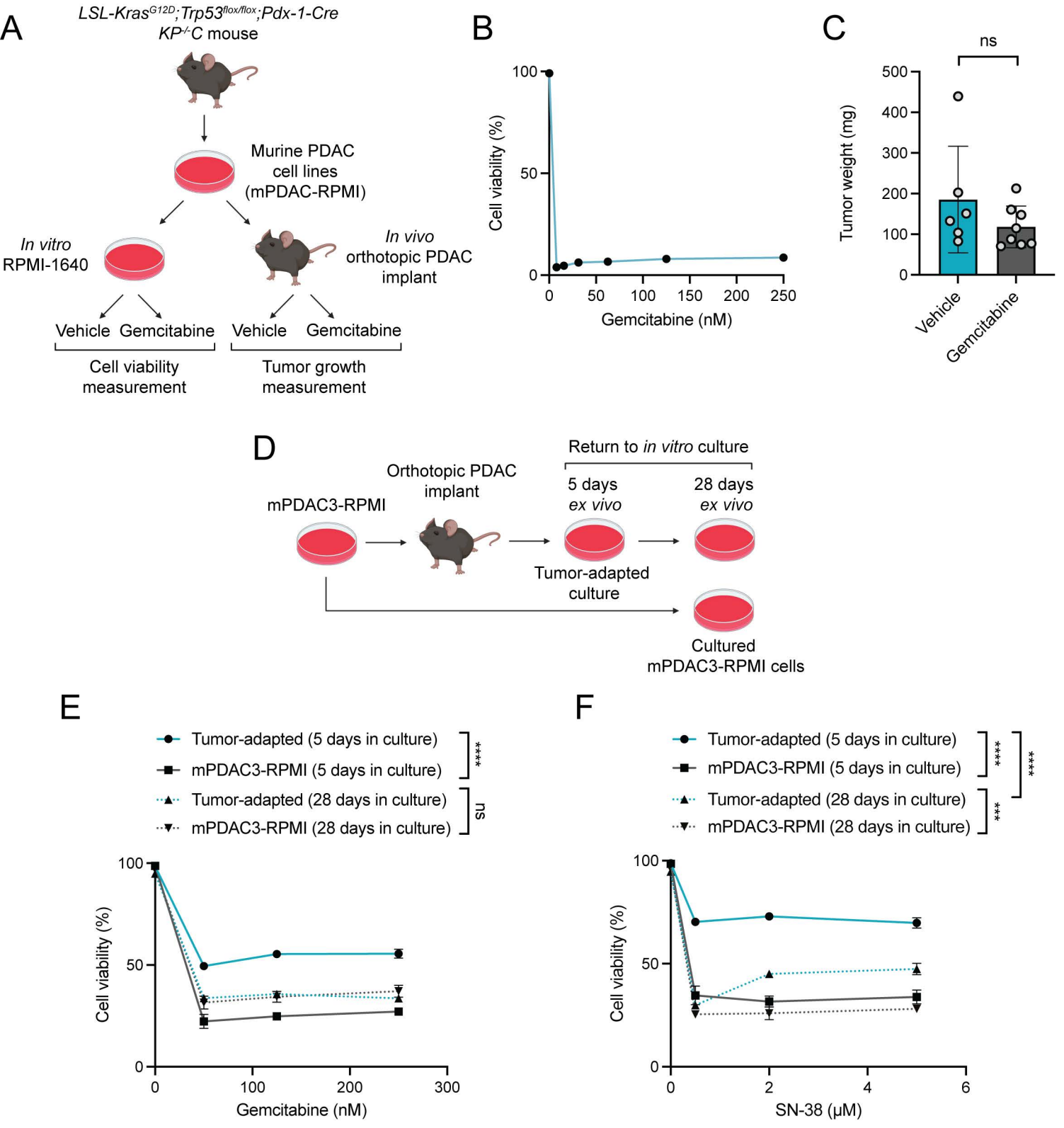
A
LSL-KrasG12D;Trp53flox/flox;Pdx-1-Cre
KP-/-C mouse
Murine PDAC
cell lines
(mPDAC-RPMI)
In vitro
RPMI-1640
In vivo
orthotopic PDAC
implant
Vehicle
Gemcitabine
Vehicle
Gemcitabine
Cell viability
measurement
Tumor growth
measurement
B
Cell viability (%)
Gemcitabine (nM)
C
ns
Tumor weight (mg)
Vehicle
Gemcitabine
D
mPDAC3-RPMI
Orthotopic PDAC
implant
Return to in vitro culture
5 days
ex vivo
28 days
ex vivo
Tumor-adapted
culture
Cultured
mPDAC3-RPMI cells
E
Tumor-adapted (5 days in culture)
mPDAC3-RPMI (5 days in culture)
Tumor-adapted (28 days in culture)
mPDAC3-RPMI (28 days in culture)
****
ns
Cell viability (%)
Gemcitabine (nM)
F
Tumor-adapted (5 days in culture)
mPDAC3-RPMI (5 days in culture)
Tumor-adapted (28 days in culture)
mPDAC3-RPMI (28 days in culture)
****
***
****
Cell viability (%)
SN-38 (μM)

Figure 2

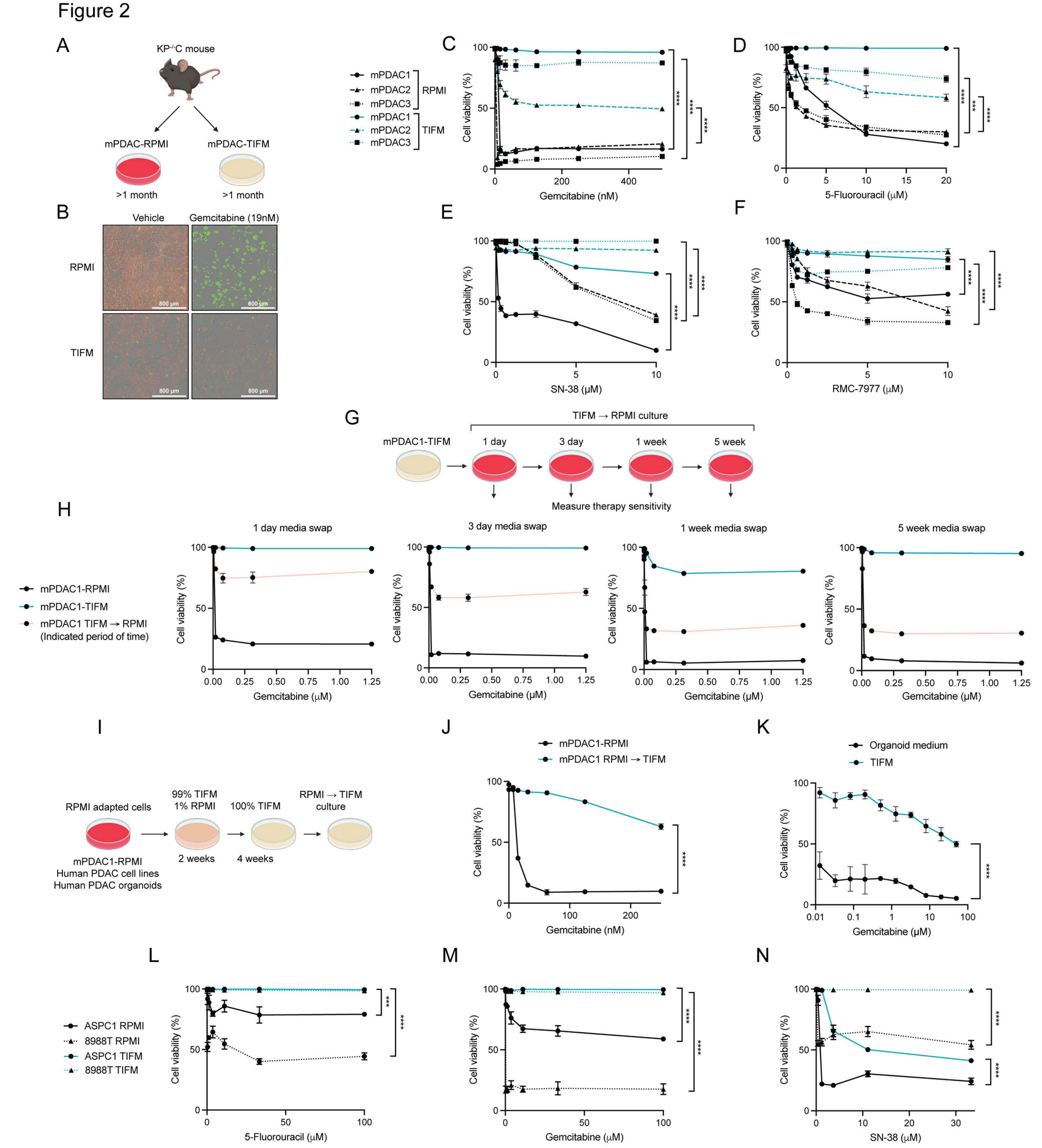
A
KP-/-C mouse
mPDAC-RPMI
mPDAC-TIFM
>1 month
>1 month
B
Vehicle
Gemcitabine (19nM)
RPMI
TIFM
800 µm
C
mPDAC1
mPDAC2
mPDAC3
RPMI
TIFM
Cell viability (%)
Gemcitabine (nM)
D
5-Fluorouracil (µM)
E
SN-38 (µM)
F
RMC-7977 (µM)
G
TIFM → RPMI culture
mPDAC1-TIFM
1 day
3 day
1 week
5 week
Measure therapy sensitivity
H
1 day media swap
3 day media swap
1 week media swap
5 week media swap
mPDAC1-RPMI
mPDAC1-TIFM
mPDAC1 TIFM → RPMI
(Indicated period of time)
Gemcitabine (µM)
I
RPMI adapted cells
99% TIFM
1% RPMI
100% TIFM
RPMI → TIFM
culture
mPDAC1-RPMI
Human PDAC cell lines
Human PDAC organoids
2 weeks
4 weeks
J
mPDAC1-RPMI
mPDAC1 RPMI → TIFM
K
Organoid medium
TIFM
L
ASPC1 RPMI
8988T RPMI
ASPC1 TIFM
8988T TIFM
M
N

Figure 2 - Figure supplement 1

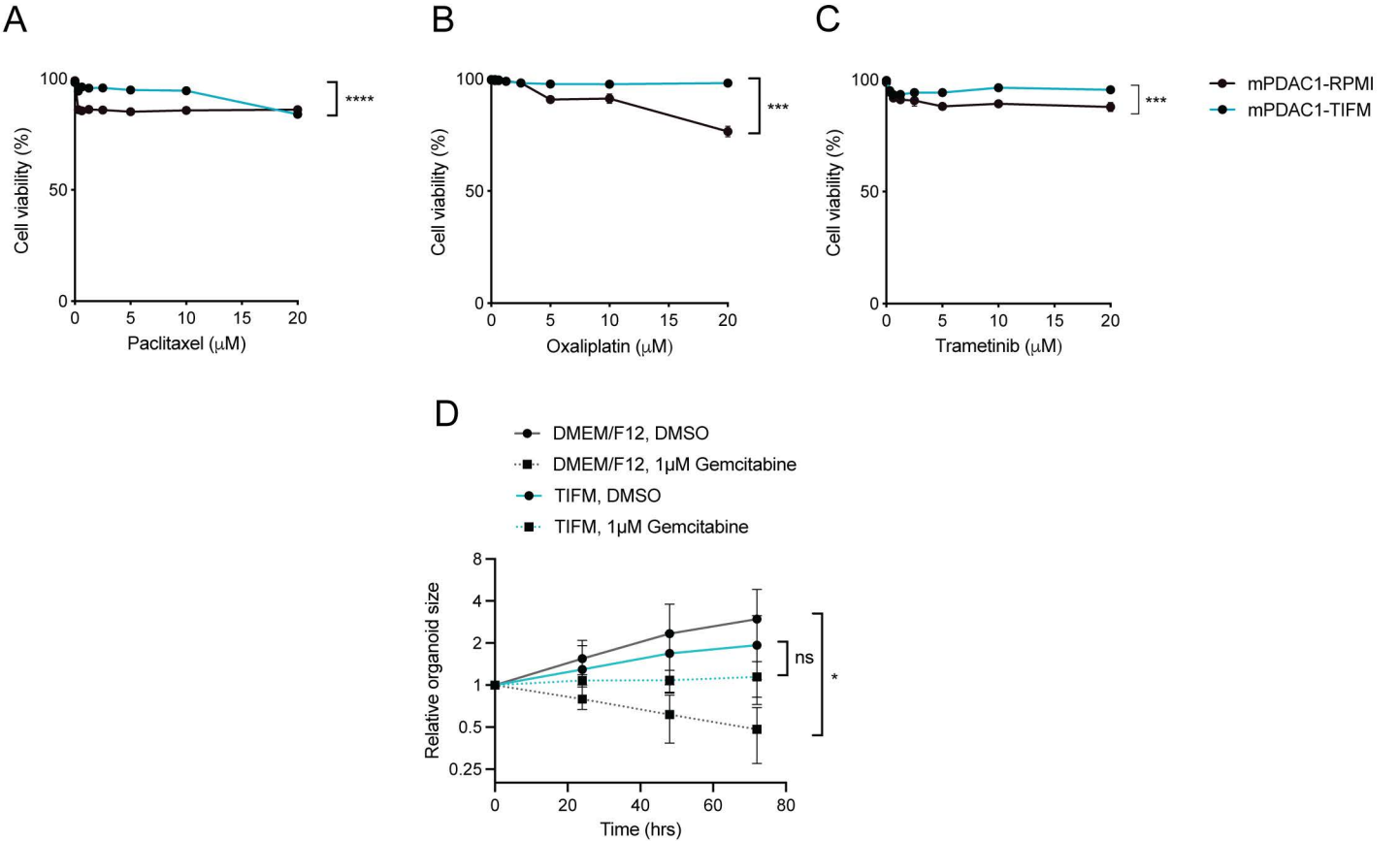

Figure 2 - Figure supplement 2

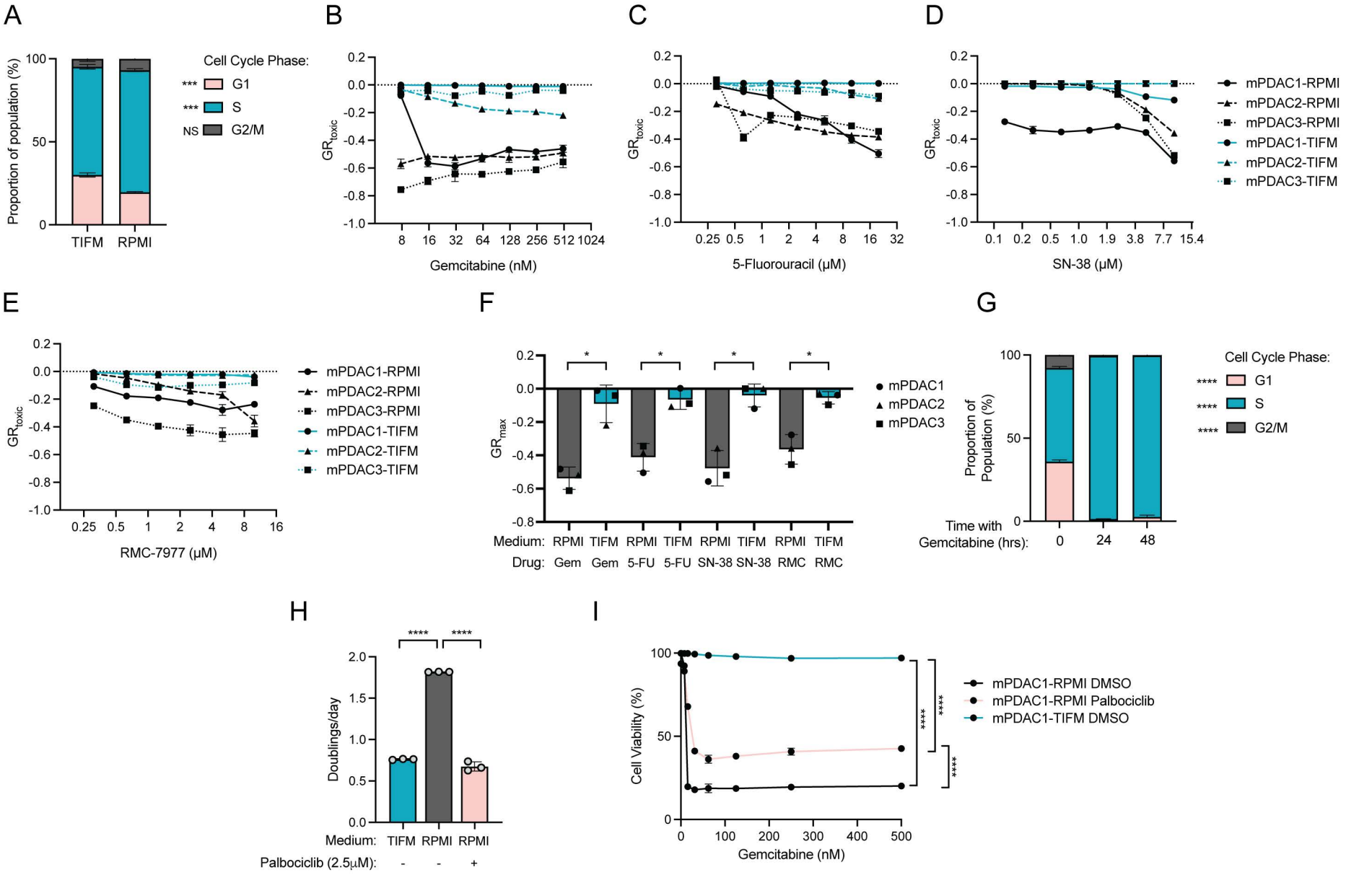

Figure 2 - Figure supplement 3

A

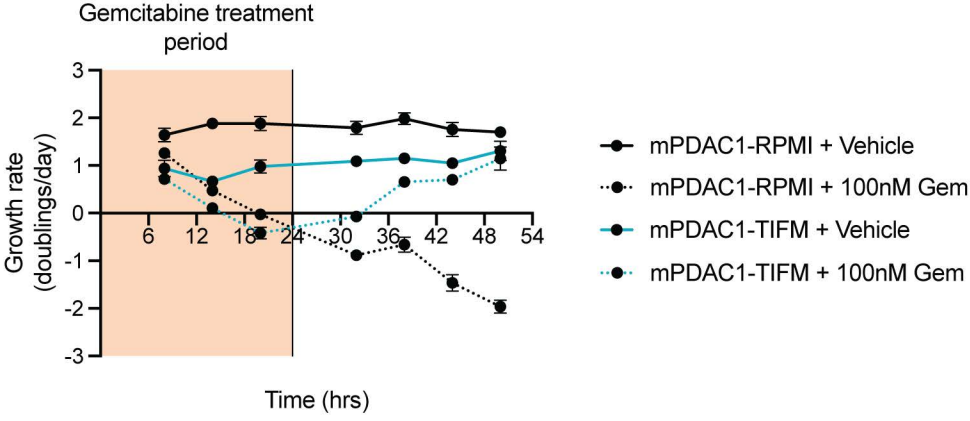

Figure 2 - Figure supplement 4 .

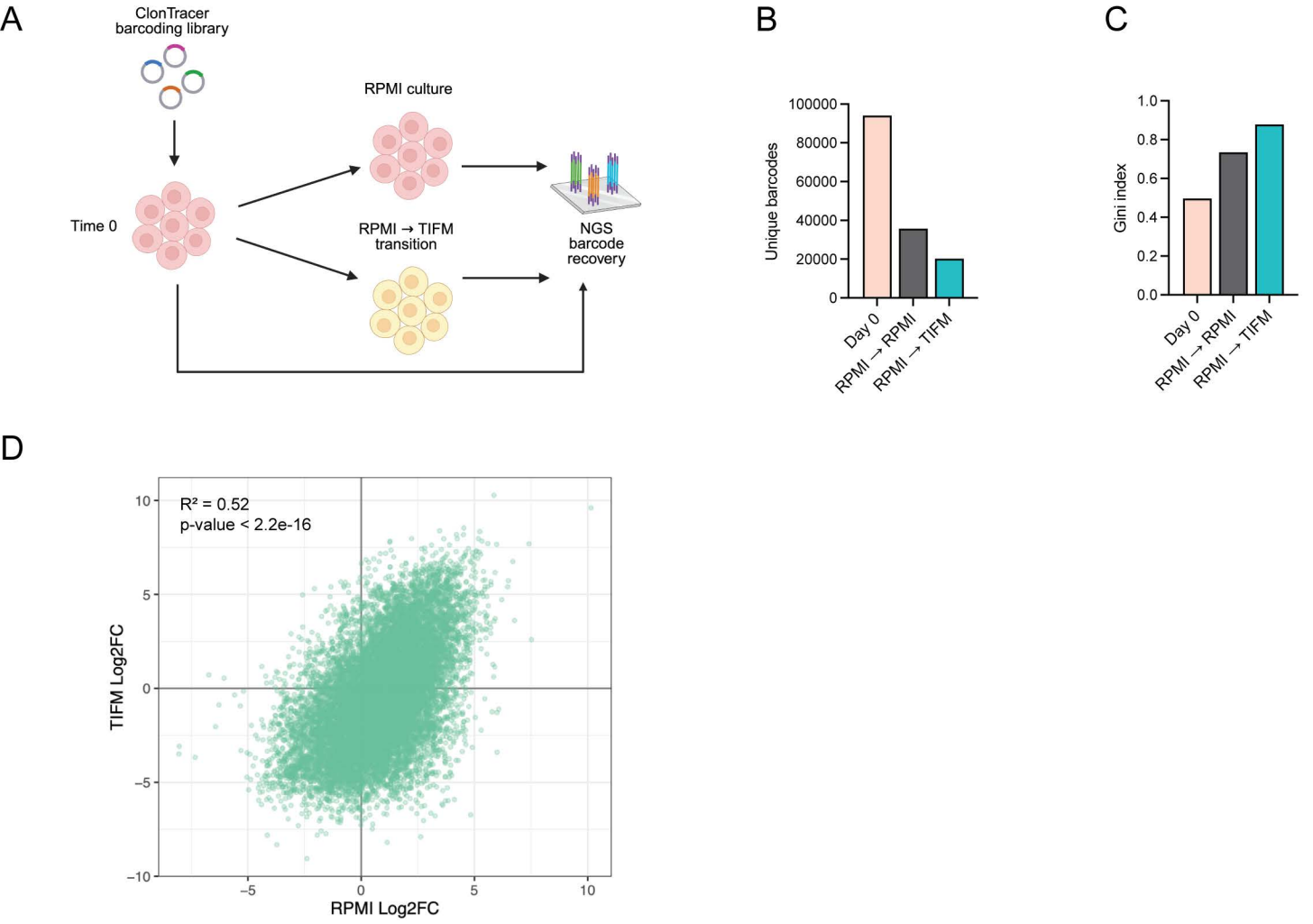

Figure 3

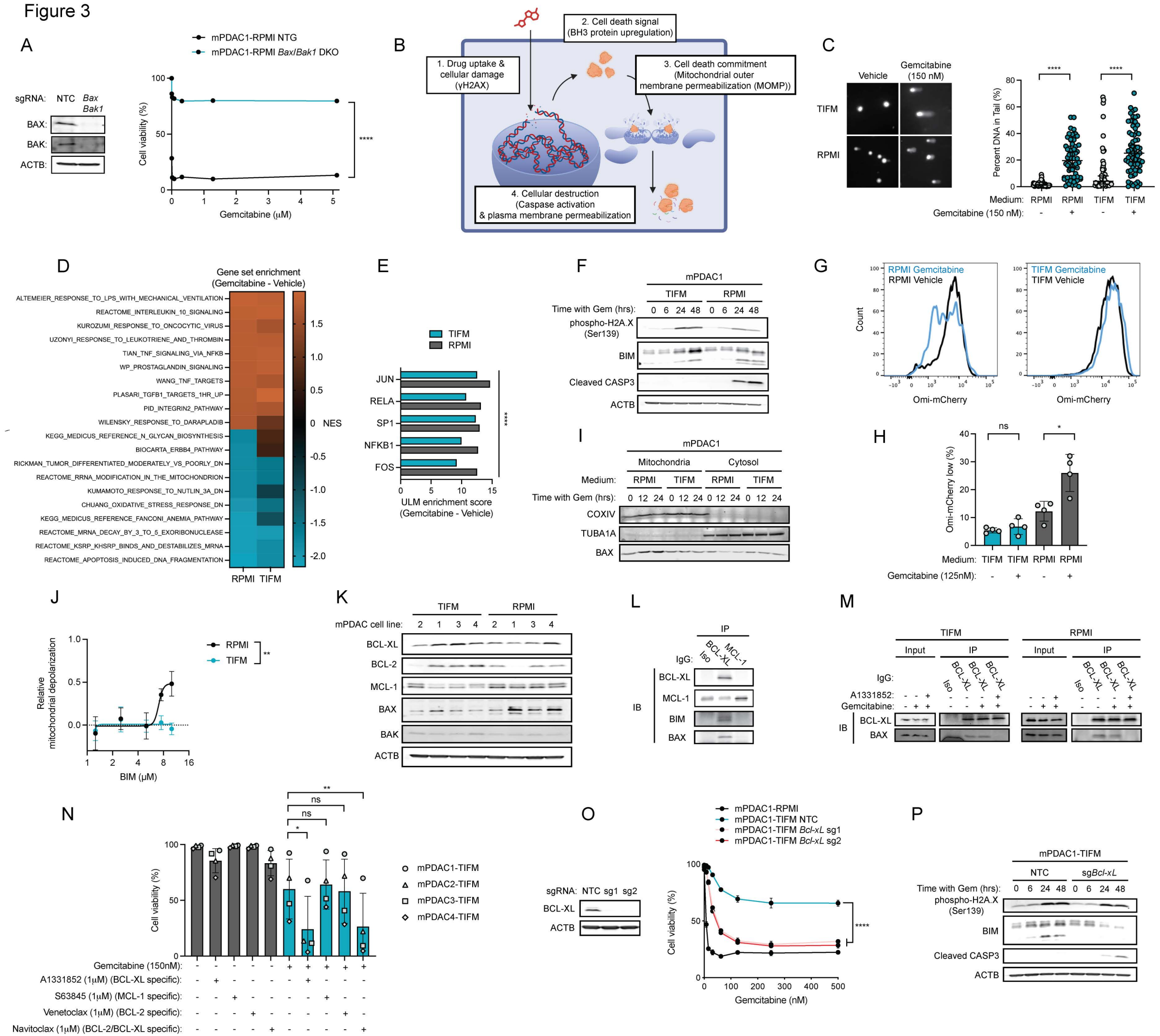
A
mPDAC1-RPMI NTG
mPDAC1-RPMI Bax/Bak1 DKO
sgRNA: NTC Bax Bak1
BAX:
BAK:
ACTB:
Cell viability (%)
Gemcitabine (μM)
****
B
1. Drug uptake & cellular damage (γH2AX)
2. Cell death signal (BH3 protein upregulation)
3. Cell death commitment (Mitochondrial outer membrane permeabilization (MOMP))
4. Cellular destruction (Caspase activation & plasma membrane permeabilization
C
Vehicle
Gemcitabine (150 nM)
TIFM
RPMI
Percent DNA in Tail (%)
Medium: RPMI RPMI TIFM TIFM
Gemcitabine (150 nM): - + - +
D
Gene set enrichment (Gemcitabine - Vehicle)
ALTEMEIER_RESPONSE_TO_LPS_WITH_MECHANICAL_VENTILATION
REACTOME_INTERLEUKIN_10_SIGNALING
KUROZUMI_RESPONSE_TO_ONCOCYTIC_VIRUS
UZONYI_RESPONSE_TO_LEUKOTRIENE_AND_THROMBIN
TIAN_TNF_SIGNALING_VIA_NFKB
WP_PROSTAGLANDIN_SIGNALING
WANG_TNF_TARGETS
PLASARI_TGFB1_TARGETS_1HR_UP
PID_INTEGRIN2_PATHWAY
WILENSKY_RESPONSE_TO_DARAPLADIB
KEGG_MEDICUS_REFERENCE_N_GLYCAN_BIOSYNTHESIS
BIOCARTA_ERBB4_PATHWAY
RICKMAN_TUMOR_DIFFERENTIATED_MODERATELY_VS_POORLY_DN
REACTOME_RRNA_MODIFICATION_IN_THE_MITOCHONDRION
KUMAMOTO_RESPONSE_TO_NUTLIN_3A_DN
CHUANG_OXIDATIVE_STRESS_RESPONSE_DN
KEGG_MEDICUS_REFERENCE_FANCONI_ANEMIA_PATHWAY
REACTOME_MRNA_DECAY_BY_3_TO_5_EXORIBONUCLEASE
REACTOME_KSRP_KHSRP_BINDS_AND_DESTABILIZES_MRNA
REACTOME_APOPTOSIS_INDUCED_DNA_FRAGMENTATION
RPMI TIFM
NES
E
TIFM
RPMI
JUN
RELA
SP1
NFKB1
FOS
ULM enrichment score (Gemcitabine - Vehicle)
****
F
mPDAC1
TIFM RPMI
Time with Gem (hrs): 0 6 24 48 0 6 24 48
phospho-H2A.X (Ser139)
BIM
Cleaved CASP3
ACTB
G
RPMI Gemcitabine
RPMI Vehicle
TIFM Gemcitabine
TIFM Vehicle
Count
Omi-mCherry
H
ns
*
Omi-mCherry low (%)
Medium: TIFM TIFM RPMI RPMI
Gemcitabine (125nM): - + - +
I
mPDAC1
Mitochondria Cytosol
Medium: RPMI TIFM RPMI TIFM
Time with Gem (hrs): 0 12 24 0 12 24 0 12 24 0 12 24
COXIV
TUBA1A
BAX
J
RPMI
TIFM
**
Relative mitochondrial depolarization
BIM (μM)
K
TIFM RPMI
mPDAC cell line: 2 1 3 4 2 1 3 4
BCL-XL
BCL-2
MCL-1
BAX
BAK
ACTB
L
IP
IgG: Iso BCL-XL MCL-1
IB
BCL-XL
MCL-1
BIM
BAX
M
TIFM RPMI
Input IP Input IP
IgG: Iso BCL-XL BCL-XL BCL-XL Iso BCL-XL BCL-XL BCL-XL
A1331852: - - + - - - + - - - +
Gemcitabine: - + + - - + + - + + - +
IB
BCL-XL
BAX
N
**
ns
ns
*
Cell viability (%)
mPDAC1-TIFM
mPDAC2-TIFM
mPDAC3-TIFM
mPDAC4-TIFM
Gemcitabine (150nM): - - - - - + + + + +
A1331852 (1μM) (BCL-XL specific): - + - - - - + - - -
S63845 (1μM) (MCL-1 specific): - - + - - - - + - -
Venetoclax (1μM) (BCL-2 specific): - - - + - - - - + -
Navitoclax (1μM) (BCL-2/BCL-XL specific): - - - - + - - - - +
O
sgRNA: NTC sg1 sg2
BCL-XL
ACTB
mPDAC1-RPMI
mPDAC1-TIFM NTC
mPDAC1-TIFM Bcl-xL sg1
mPDAC1-TIFM Bcl-xL sg2
Cell viability (%)
Gemcitabine (nM)
****
P
mPDAC1-TIFM
NTC sgBcl-xL
Time with Gem (hrs): 0 6 24 48 0 6 24 48
phospho-H2A.X (Ser139)
BIM
Cleaved CASP3
ACTB

Figure 3 - Figure supplement 1

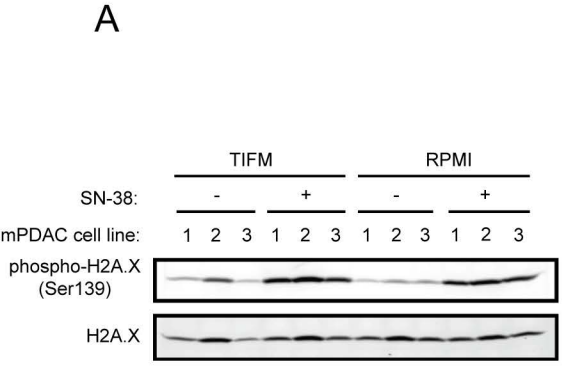

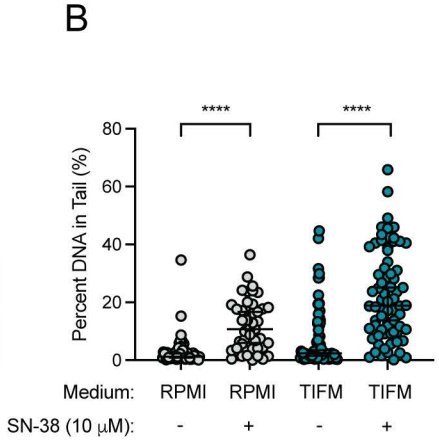

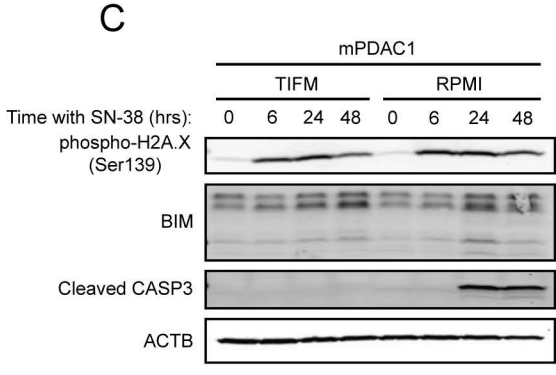

Figure 3 - Figure supplement 2

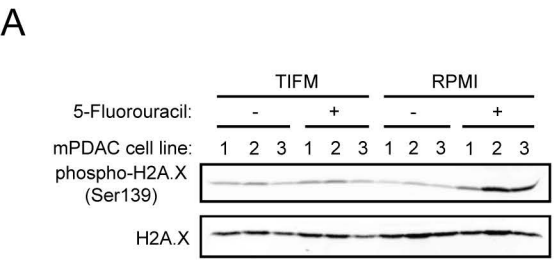

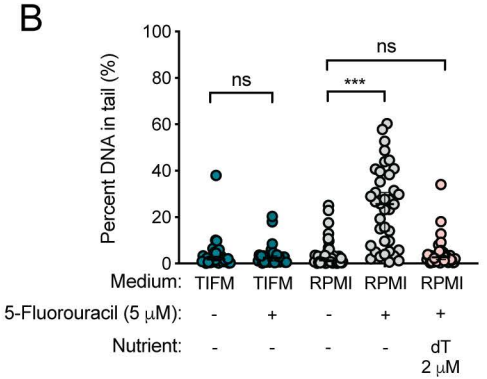

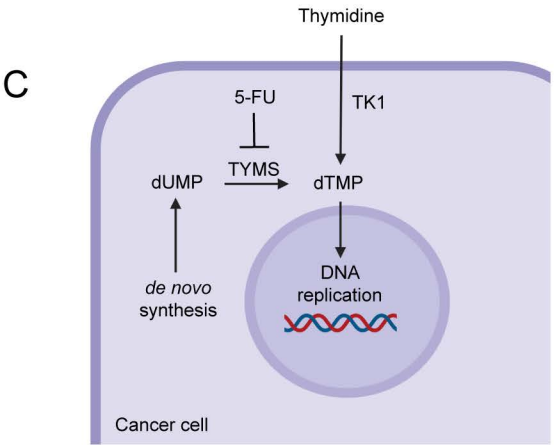

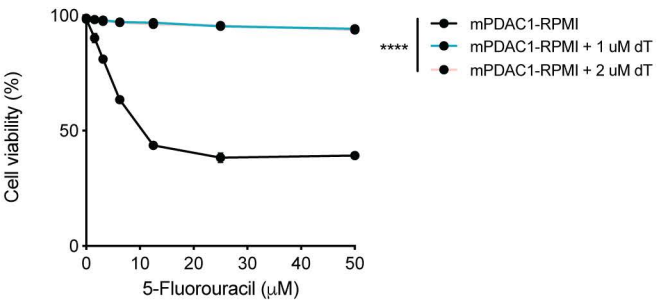

Figure 3-Figure Supplement 3

A

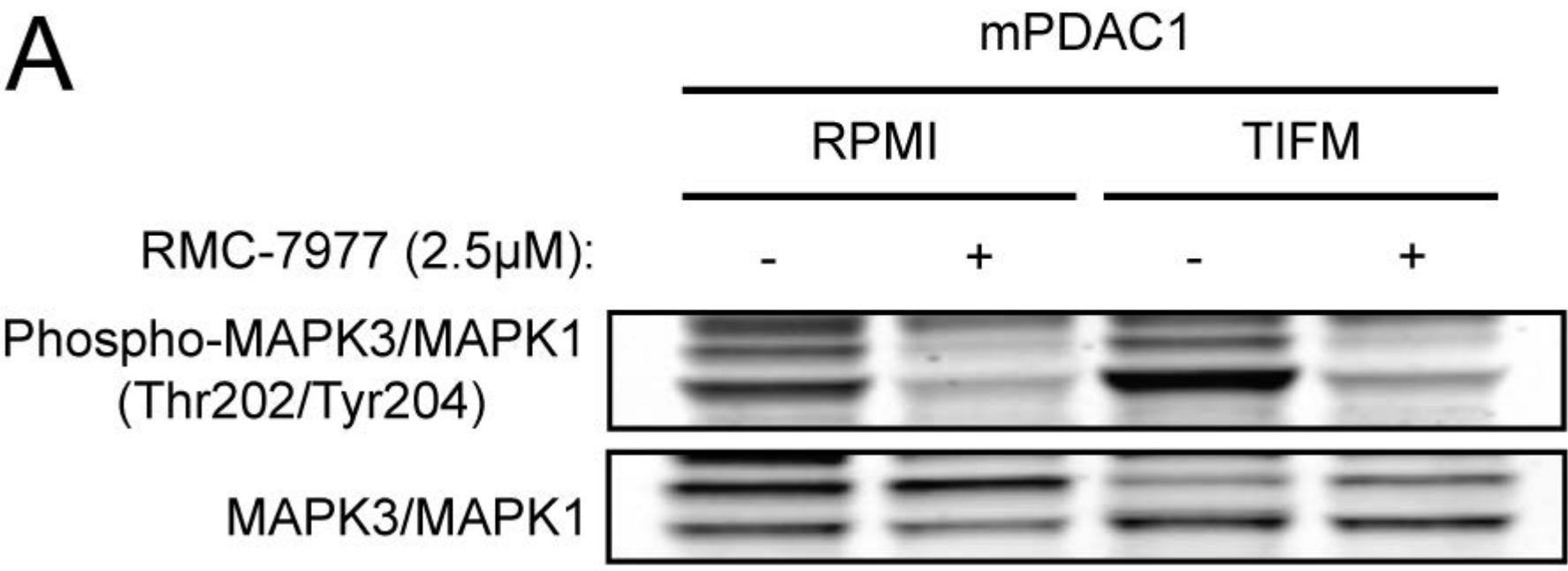

Figure 3 - Figure supplement 4

A

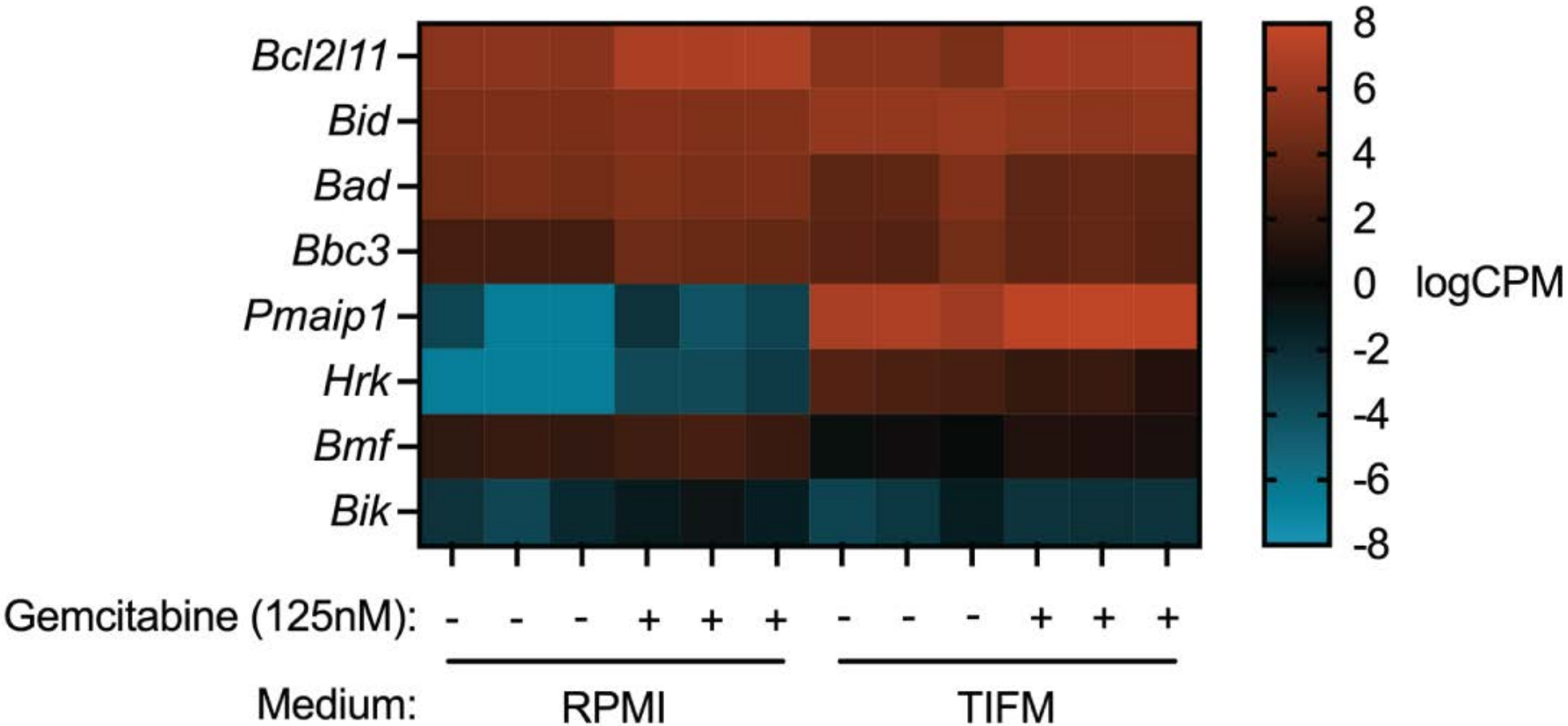

Figure 3 - Figure supplement 5

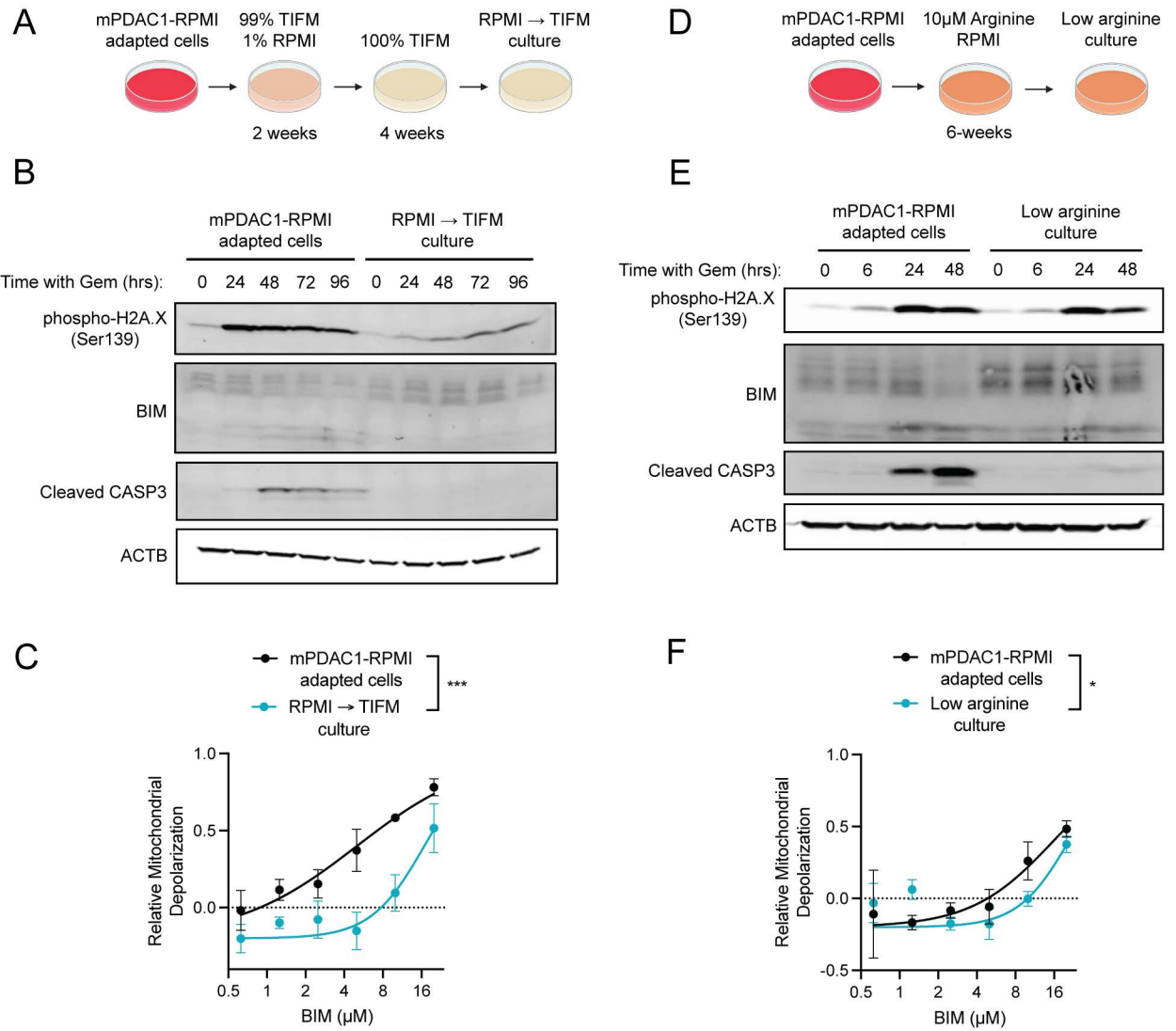

Figure 3 - Figure supplement 6

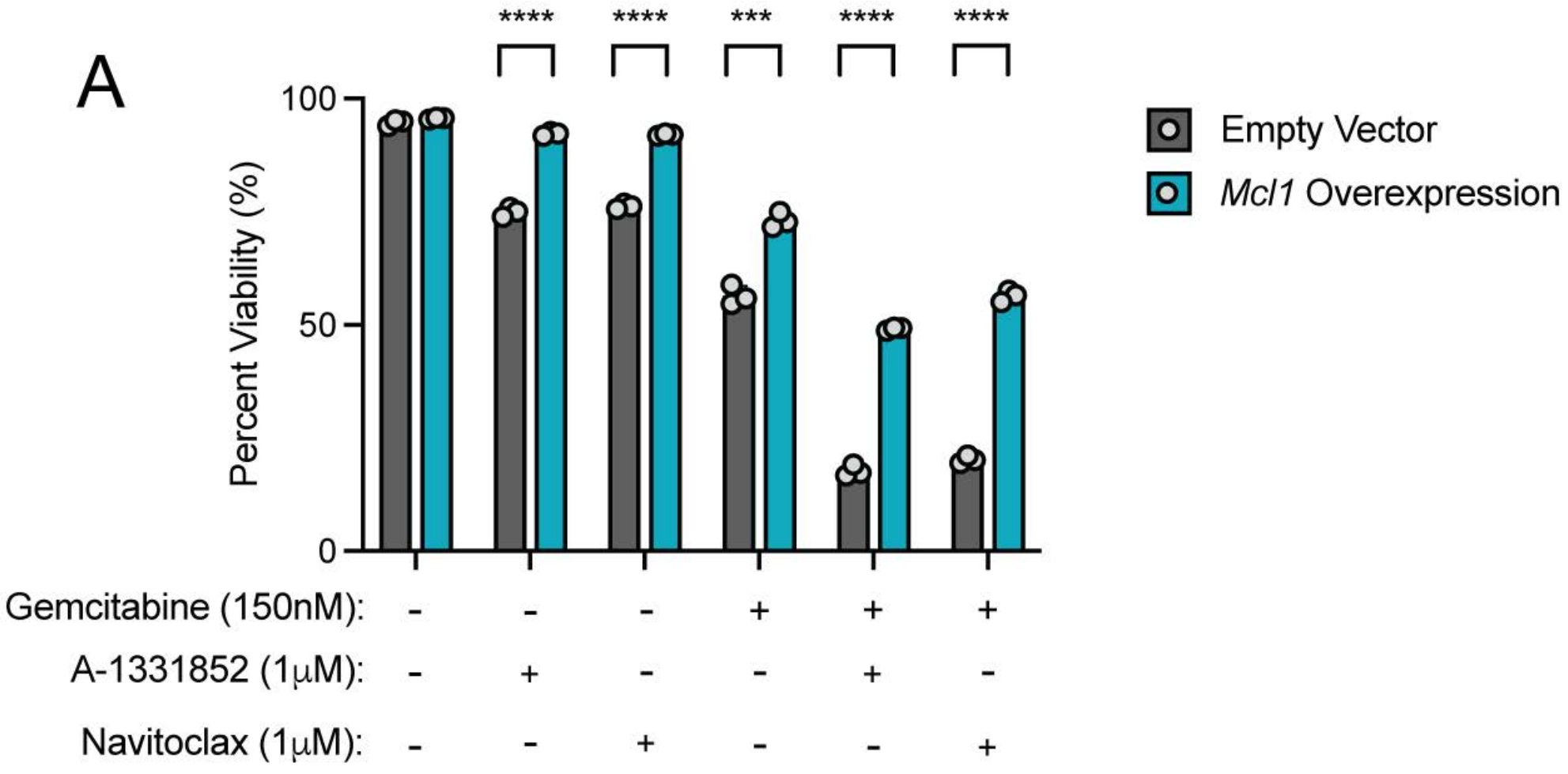

Figure 4

A

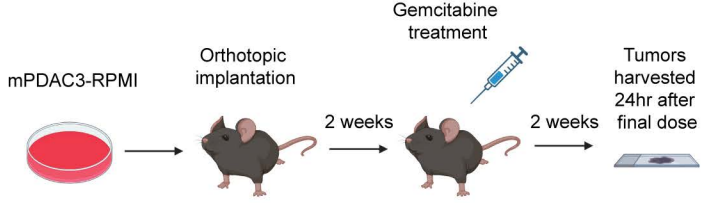

B

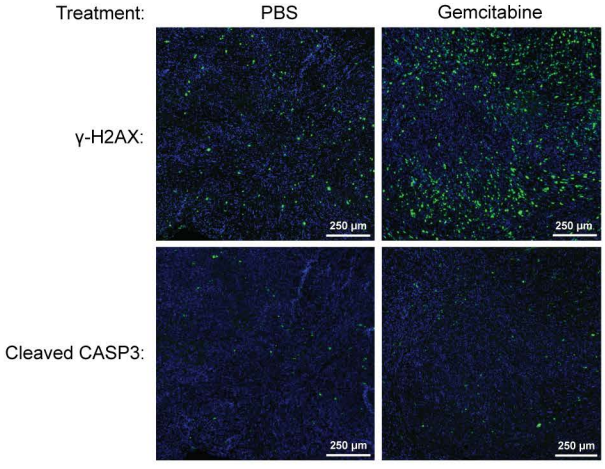

C

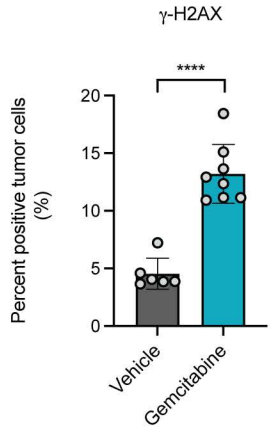

D

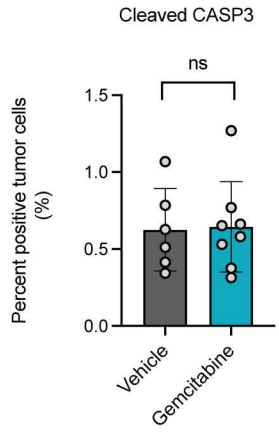

E

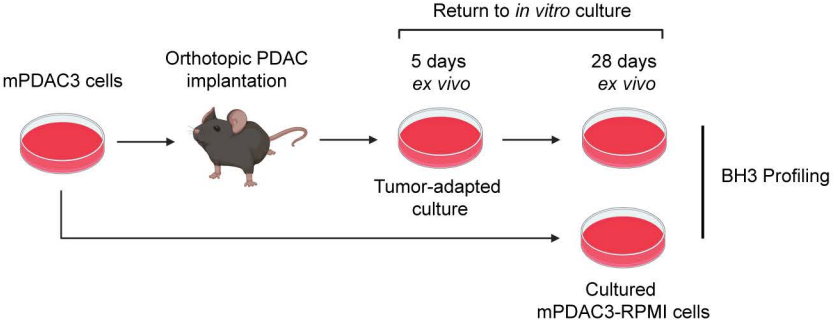

F

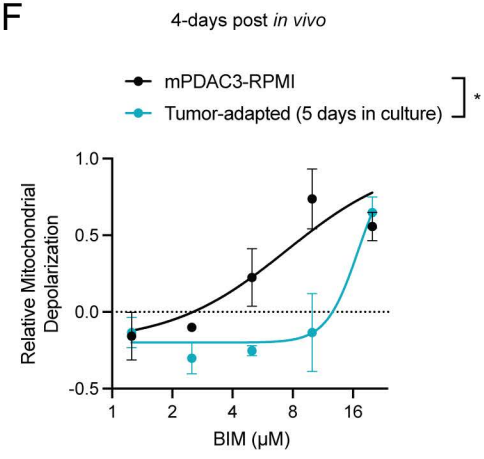
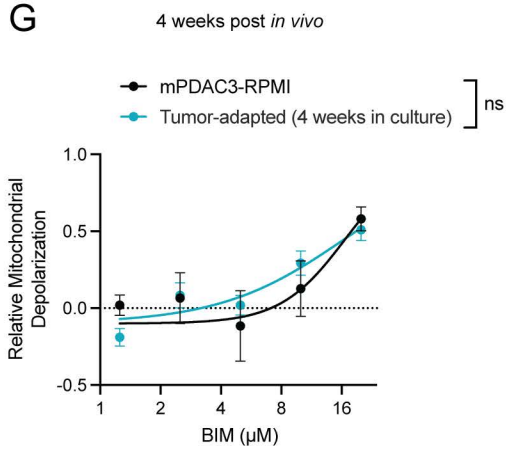
G